
# Joint spatial modeling of significant wave height and wave period using the SPDE approach

Probabilistic Engineering Mechanics 68 (2022) 103203

Contents lists available at ScienceDirect

Probabilistic Engineering Mechanics

journal homepage: www.elsevier.com/locate/probengmech

# Joint spatial modeling of significant wave height and wave period using the SPDE approach

Anders Hildeman [a,*], David Bolin [b], Igor Rychlik [c]

[a] Department of Space, Earth and Environment, Chalmers University of Technology, Sweden
[b] Computer, Electrical and Mathematical Science and Engineering Division, King Abdullah University of Science and Technology, Saudi Arabia
[c] Department of Mathematical Sciences, Chalmers University of Technology and University of Gothenburg, Sweden

ARTICLE INFO

*Keywords:*
SPDE approach
Non-stationary Gaussian random fields
Significant wave height
Wave period
Stochastic weather generator

ABSTRACT

The ocean wave distribution in a specific region of space and time is described by its sea state. Knowledge about the sea states a ship encounters on a journey can be used to assess various parameters of risk and wear associated with this journey. Two important characteristics of the sea state are significant wave height and mean wave period. We propose a joint spatial model of these two quantities on the north Atlantic ocean. The model describes the distribution of the logarithm of the two quantities as a bivariate Gaussian random field, modeled as a solution to a system of coupled fractional stochastic partial differential equations. The bivariate random field is non-stationary and allows for arbitrary, and different, smoothness for the two marginal fields.

The parameters of the model are estimated from data using a stepwise maximum likelihood method. The fitted model is used to derive the distribution of accumulated fatigue damage for a ship sailing a transatlantic route. Also, a method for estimating the risk of capsizing due to broaching-to based on the joint distribution of the two sea state characteristics is investigated. The risks are calculated for a transatlantic route between America and Europe using both data and the fitted model. The results show that the model compares well with observed data. It further shows that the bivariate model is needed and cannot simply be approximated by a model of significant wave height alone.

## 1. Introduction

The sea state characterizes the stochastic behavior of ocean waves in a region in space and time. Explicit knowledge of the sea state allows for quantitative assessments of profits, costs, and risks associated with naval logistics, fishing, marine operations, and other applications affected by the sea surface conditions.

Let us denote the spatio-temporal stochastic process of sea surface elevation as $W(s,t)$, where $s \in \mathcal{G}$, $t \in [0,\mathcal{T}]$. Here, $\mathcal{G}$ is a small region in space and $[0,\mathcal{T}]$ is a small interval in time, typically from 20 min up to about 3 h. The distribution of $W$ is equivalent to the sea state at $\mathcal{G}\times[0,\mathcal{T}]$. In general, a spatio-temporal stochastic process can be very complex to model. However, for waves in deep water the sea surface elevation can often be adequately approximated by Gaussian random fields. Furthermore, if $\mathcal{G}$ and $\mathcal{T}$ are small enough, $W$ will be a stationary Gaussian process. For applications related to floating structures, such as ships, the deviations of sea elevation from the mean sea level is of interest. Hence, $W$ could be modeled as a centered stationary Gaussian process and is therefore completely characterized by the directional spectrum $S(\omega,\theta)$. Here $\omega \geq 0$ is the angular frequency of the waves and $\theta \in [0,2\pi]$ is the direction [1].

In this paper our main concern are applications related to ship safety. For such applications we are mainly interested in sea states where a dominant part of the wave energy is propagating in a narrow band of directions, a so called *long crested sea*. Hence, we will make the approximation $S(\omega,\theta) = S(\omega)\delta(\theta-\theta_0)$, where $S(\omega) = \int_0^{2\pi} S(\omega,\theta)d\theta$ is the temporal spectrum, $\theta_0$ is the direction the waves are propagating from, and $\delta$ is the Dirac delta function. For a *long crested sea* the sea state is completely characterized by its temporal spectrum and a wave direction.

For most applications a few scalar valued quantities are enough to characterize the temporal spectrum. One such example is the popular Bretschneider spectrum [2], which has been shown to explain the important characteristics of sea states for a wide range of applications and spatial regions. This spectrum is fully characterized by the *significant wave height* $H_s$ and the *peak wave period* $T_p$. The Bretschneider spectrum is defined as

$$S(\omega) = c\omega^{-5}\exp\left(-1.25\frac{\omega_p^4}{\omega^4}\right), \qquad c = \frac{1.25}{4}H_s^2\omega_p^4, \qquad \omega_p = 2\pi/T_p.$$

Here, $H_s = 4\sqrt{\mathrm{Var}[W(s,t)]}$ is four times the standard deviation of the sea surface elevation. It is a quantity summarizing the distribution of

* Corresponding author.
*E-mail address:* hildeman@chalmers.se (A. Hildeman).

https://doi.org/10.1016/j.probengmech.2022.103203
Received 14 November 2019; Received in revised form 15 April 2021; Accepted 24 January 2022
Available online 9 February 2022

wave heights of apparent waves and is measured in units of length, in this paper in meters [m]. The significant wave height is in general the most important single quantity when assessing risks to ships in a given sea state. Another important quantity is the *peak wave period*. It is defined as the wave period with the highest energy,

$$T_p = \frac{2\pi}{\arg\max_{\omega>0} S(\omega)},$$

and summarizes the distribution of wave periods of apparent waves. It is measured in units of time, in our paper in seconds [s]. Two other popular quantities summarizing the distribution of wave periods are the *mean wave period*, $T_1$, and *mean zero-crossing period*, $T_z$, defined as

$$T_1 = 2\pi \frac{\int_0^\infty S(\omega)d\omega}{\int_0^\infty \omega\, S(\omega)d\omega}, \qquad T_z = 2\pi\sqrt{\frac{\int_0^\infty S(\omega)d\omega}{\int_0^\infty \omega^2\, S(\omega)d\omega}}.$$

In words, $T_1$ averages over frequencies while $T_z$ is the mean time between a zero upcrossing and the consecutive one for a fixed point in space. Under the assumption of a Bretschneider spectrum, these three quantities are related as $T_p = 1.408 \cdot T_z = 1.2965 \cdot T_1$ [3]. Since all three quantities are proportional to each other under the assumption of a Bretschneider spectrum we will use the notation $T$ to denote a quantity of the wave period without explicitly stating which. Hence, as long as the Bretschneider spectrum is a reasonable approximation all information about the sea state is encoded in the two quantities $H_s$ and $T$.

One problem with modeling the random field using a spectrum is that it assumes stationarity, i.e., the same distributional behavior for all locations in space and time. This is typically not valid for large spatial/temporal regions. Hence, it is often assumed that the stationary model explains the wave distribution on small scales while the parameters $H_s$ and $T$ are spatially/temporally varying, in this way allowing for different distributions of apparent waves at different points in space–time.

The main contribution of this work is to propose a joint spatial model for $H_s$ and $T$ which can be used to describe the sea state variations over large regions, where stationarity cannot necessarily be assumed. It should be mentioned that our model does not assume a Bretschneider spectrum. However, we will assume a Bretschneider spectrum later in Section 6 where some examples of possible usages of such a sea state model are provided.

Probabilistic models of $H_s$ and $T$ jointly for a fixed point in space and time have been studied extensively. Ochi [4] showed that a bivariate log-normal distribution fits the bulk of the marginal probability distributions of $H_s$ and $T$ for data from the north Atlantic. Other approaches are to use Placket-models [5,6], or more general Box–Cox transformations [7], and then model the transformed values with a bivariate Gaussian distribution. Conditional modeling approaches have also been proposed where $H_s$ is first modeled and $T$ is later modeled conditioned on $H_s$ [8–10]. Also temporal models for $H_s$ and/or $T$ for a fixed point in space have been studied. These models are often based on transformations of the marginal data to Gaussianity such that the temporal correlation can be modeled by ARMA-processes [11, and the reference within]. Further complexity can be added on top of that by modeling a storm/non-storm dichotomy through a latent Poisson-style process [12,13].

As stated above, we are in this work interested in spatial models for $H_s$ and $T$ (and in extension spatio-temporal models), such models are important when considering moving ships where the wave state at points visited on the ships route will be highly dependent. An important property of a spatial model for any larger region is that it allow for spatial non-stationarity [14]. Some prior work on modeling $H_s$ spatially, or spatio-temporally, using transformed Gaussian random fields exist. Such spatial models are usually based on a chosen parametric stationary covariance function for which parameters are estimated using maximum likelihood, posterior distributions and/or minimum contrast methods. Baxevani et al. [15] considered regions small enough to assume stationarity in order to work with a stationary Gaussian model. To handle non-stationarity this model was later extended by Baxevani et al. [14] to a spatial moving average process with a non-stationary Gaussian kernel and drift. A similar drift model but with a rational quadratic covariance function was used in Ailliot et al. [16].

In Hildeman et al. [17] a non-stationary and anisotropic model was proposed based on the SPDE approach [18] and the deformation method [19]. Compared to the covariance-based models of [15,14,16] this model is based on a description of the random field through a stochastic partial differential equation (SPDE). Approaching the characterization of the random field from an SPDE perspective has some distinct benefits. For example, it facilitates modeling on complex spatial domains, simplifies the introduction of non-stationarity, and can be used to reduce the computational cost of inference and sampling.

The model we propose in this work is an extension of the model for $H_s$ by Hildeman et al. [17]. Specifically, we will assume that the joint distribution of $H_s$ and $T$ is Gaussian after logarithmic transformation of both variables, as proposed by Ochi [4]. We will then model $\log(H_s)$ and $\log(T)$ using a bivariate extension of the model by Hildeman et al. [17] where we also allow for arbitrary smoothness of the two random fields as well as a spatially varying cross-correlation of the two quantities.

The proposed model is purely spatial, not spatio-temporal. Hence, it assumes that the probability distribution in space is the same for all point in time. Such an assumption is not viable over the whole year due to seasonal variations. We therefore focus on one month at a time, approximating the spatial distribution during the course of a month to be stationary in time. In this work, 39 years of data from the north Atlantic during the month of April will be used to estimate the model, as well as to validate it. In order to avoid making this work too complex we choose to present the results for one single month, in this case April. However, note that we could just as well have chosen another month in our examples. To illustrate the flexibility of the proposed model we will show how it can be used in two separate applications of naval logistics, namely fatigue damage modeling of ships and estimation of the risk of capsizing due to broaching-to.

The structure of the paper is as follows. In Section 2 the proposed model is introduced. Section 3 describes the finite-dimensional discretization of the model that is needed for inference and simulation. In Section 4 the data used for parameter estimation and validation of the model is described. Section 5 goes through the method of estimating the parameters of the model from the available data, and presents an assessment of the model fit. Section 6 introduces two applications where the model can be used to estimate risks and wear associated with a planned ship journey. Finally, Section 7 concludes with a discussion of the results and future extensions.

## 2. Model formulation

As stated above, the goal of this work is to develop a joint spatial model of significant wave height and wave period. We base this model on the non-stationary model of Hildeman et al. [17], which has already been applied successfully to model the spatial distribution of significant wave height in the North Atlantic.

The original model is defined by interpreting $X(\boldsymbol{s}) = \log(H_s(\boldsymbol{s}))$ as a solution to the SPDE

$$\kappa(\boldsymbol{s})\mathcal{L}^{\alpha/2}\left(\tau(\boldsymbol{s})\,\mathrm{X}(\boldsymbol{s})\right) := \kappa(\boldsymbol{s})\left[I - \kappa(\boldsymbol{s})^{-2}\nabla\cdot H(\boldsymbol{s})\nabla\right]^{\alpha/2}\left(\tau(\boldsymbol{s})\,\mathrm{X}(\boldsymbol{s})\right) = \mathcal{W}(\boldsymbol{s}), \tag{1}$$

defined on a spatial domain $\mathcal{G} \subset \mathbb{R}^d$ with $d = 2$. Here, $\mathcal{W}$ is Gaussian white noise, $H$ a symmetric and positive definite matrix-valued function, $\kappa$ and $\tau$ strictly positive real-valued functions, and $\alpha > d/2$ a constant.

Defining random field models as solutions to a stochastic partial differential equation (the SPDE-approach) is an alternative way of

defining the covariance structure of a Gaussian random field implicitly through the way the solution to a stochastic differential equation smooths out a white noise process. The particular SPDE of (1) has its origin in the fact that when $\mathcal{G} := \mathbb{R}^d$, $\kappa(\boldsymbol{s}) := \kappa > 0$, $\tau(\boldsymbol{s}) := \tau > 0$, and $H(\boldsymbol{s}) := I$ is the identity matrix, a mean-zero Gaussian random field with a Matérn covariance function [20] is a solution to (1). Defining the model through the SPDE has the benefits of allowing it to be extended to arbitrary Riemannian manifolds. It also facilitates the introduction of non-stationarity by allowing the parameters to be function-valued and introduces important computational benefits [18].

In Hildeman et al. [17] it was noted that a spatial model for significant wave height needs to be able to explain spatial non-stationary and/or anisotropic behavior. To accomplish this the model was extended by the deformation method [19], i.e., a differentiable and bijective mapping, $\mathrm{F}^{-1}(\boldsymbol{s})$, maps points on the observational domain, $\mathcal{G}$, to points on a subset to some manifold, $\mathcal{D}$. By considering a Matérn covariance structure in $\mathcal{D}$ (the *deformed space*) one can acquire a non-stationary or anisotropic random field in the observable space, $\mathcal{G}$. The parameters $\kappa(\boldsymbol{s})$ and $H(\boldsymbol{s})$ of the model are functions of the deformation. Specifically, $\tilde{X}(\tilde{\boldsymbol{s}}) := X(\mathrm{F}^{-1}(\boldsymbol{s}))$ is a unit-variance Gaussian random field with a Matérn covariance function with the same smoothness parameter, $\alpha$, as in (1). Because of this, the function F explains the anisotropy, non-stationarity, and correlation range of $X$, whereas $\tau(\boldsymbol{s})$ determines the marginal variances, and $\alpha$ the smoothness.

The connection between the parameters $H(\boldsymbol{s}), \kappa(\boldsymbol{s})$ of the SPDE in (1) and the mapping $\mathrm{F} : \mathcal{D} \mapsto \mathcal{G}$ is

$$\kappa^2(\boldsymbol{s}) = \left|J[\mathrm{F}^{-1}](\boldsymbol{s})\right|, \quad H(\boldsymbol{s}) = \kappa^2(\boldsymbol{s}) J[\mathrm{F}^{-1}]^{-1}(\boldsymbol{s}) J[\mathrm{F}^{-1}]^{-T}(\boldsymbol{s}),$$

where $J[F^{-1}]$ denotes the Jacobian matrix of $F^{-1}$. This means that the SPDE is completely characterized by the Jacobian matrix of $F$ together with $\alpha$ and $\tau$. In fact, the model is well-defined for a broader class than those which are truly diffeomorphic to a Matérn Gaussian random field—it is enough that they are locally diffeomorphic to a Matérn Gaussian random field. That is, any $d \times d$ matrix-valued function which is Lipschitz continuous and uniformly positive definite (or uniformly negative definite) can be used in place of $J[F^{-1}]$. This means that a true $\mathcal{D}$-space does not have to exist. The $\mathcal{D}$-space is just a construct used to acquire the correct SPDE (1) for $\mathcal{G}$-space.

In Hildeman et al. [17] it was shown that this SPDE model agreed well with data of significant wave height in the north Atlantic ocean. We now extend the model to a bivariate random field for probabilistic modeling of significant wave height and wave period jointly. We construct a bivariate model for which the distributions $H_s$ and $T$ separately are both part of the class of models defined by (1). Let us denote $X(\boldsymbol{s}) := \log H_s(\boldsymbol{s})$ and $Y(\boldsymbol{s}) := \log T(\boldsymbol{s})$, and consider $X$ and $Y$ as dependent Gaussian random fields. Bolin and Wallin [21],Hu et al. [22],Hu and Steinsland [23] developed multivariate models of Gaussian random fields based on a triangular system of SPDEs. Inspired by those models we could extend (1) to a bivariate model as,

$$\begin{bmatrix} g_{11} & g_{12} \\ 0 & g_{22} \end{bmatrix} \begin{bmatrix} \kappa_X \mathcal{L}_X^{\alpha/2} & 0 \\ 0 & \kappa_Y \mathcal{L}_Y^{\beta/2} \end{bmatrix} \begin{bmatrix} X \\ Y \end{bmatrix} =: D \begin{bmatrix} \kappa_X \mathcal{L}_X^{\alpha/2} & 0 \\ 0 & \kappa_Y \mathcal{L}_Y^{\beta/2} \end{bmatrix} \begin{bmatrix} X \\ Y \end{bmatrix} = \begin{bmatrix} \mathcal{W} \\ \mathcal{V} \end{bmatrix}.$$

Here $\mathcal{W}$ and $\mathcal{V}$ are independent and identically distributed Gaussian white noise on $\mathcal{G}$ and $g_{11}, g_{12}$, and $g_{22}$ are real-valued where $g_{11}$ and $g_{22}$ are bounded away from 0 such that $D$ is invertible. The pseudo-differential operators $\mathcal{L}_X$ and $\mathcal{L}_Y$ are defined as in (1) and control the marginal distributions of $X$ and $Y$ respectively. The term $g_{12}$ will introduce dependence between $X$ and $Y$. The inverse, $R = D^{-1}$ can be used to rewrite the system of SPDEs as

$$\begin{bmatrix} \kappa_X \mathcal{L}_X^{\alpha/2} & 0 \\ 0 & \kappa_Y \mathcal{L}_Y^{\beta/2} \end{bmatrix} \begin{bmatrix} X \\ Y \end{bmatrix} = R \begin{bmatrix} \mathcal{W} \\ \mathcal{V} \end{bmatrix} := \begin{bmatrix} h_{11} & h_{12} \\ 0 & h_{22} \end{bmatrix} \begin{bmatrix} \mathcal{W} \\ \mathcal{V} \end{bmatrix},$$

which corresponds to a linear model of coregionalization [21]. The parameters $h_{11}, h_{12}$ and $h_{22}$ are here functions of the spatial location, fully defined by the parameters in the elements of $D$. In particular, $h_{12}$ solely defines the dependency between the two fields. Moreover, considering only one random field at a time, they will have the same distribution as in the univariate case if $h_{11}^2 + h_{12}^2 = h_{22}^2 = 1$. Bolin and Wallin [21] gives a parameterization of $R$ using only one parameter, $\rho$, due to the sum-to-one constraint. The parameter $\rho \in \mathbb{R}$ controls the correlation between the fields $X$ and $Y$ but is in general not equal to the Pearson correlation coefficient. Using $\rho$, the parameters of $D$ and $R$ are fully identified as,

$$R = \begin{bmatrix} h_{11} & h_{12} \\ 0 & h_{22} \end{bmatrix} = \frac{1}{\sqrt{1+\rho^2}} \begin{bmatrix} 1 & \rho \\ 0 & \sqrt{1+\rho^2} \end{bmatrix},$$

$$D = R^{-1} = \begin{bmatrix} g_{11} & g_{12} \\ & g_{22} \end{bmatrix} = \begin{bmatrix} \sqrt{1+\rho^2} & -\rho \\ 0 & 1 \end{bmatrix}.$$

We use this parameterization but extend the model by allowing $\rho$ to be a spatially varying function. Hence, the model we consider is the following system of SPDEs

$$\begin{aligned} \sqrt{1+\rho^2}\kappa_X \mathcal{L}_X^{\alpha/2} X - \rho \kappa_Y \mathcal{L}_Y^{\beta/2} Y &= \mathcal{W} \\ \kappa_Y \mathcal{L}_Y^{\beta/2} Y &= \mathcal{V}. \end{aligned} \tag{2}$$

In the case when $\kappa_X \mathcal{L}_X^{\alpha/2} = \kappa_Y \mathcal{L}_Y^{\beta/2}$ and $\rho$ is constant the correlation coefficient between the two fields equals $\frac{\rho}{\sqrt{1+\rho^2}}$, in the sense that it corresponds to the Pearson correlation coefficient between the two fields at any fixed point in $\mathcal{G}$. In the general case the interpretation of $\rho$ as controlling the correlation still holds and values near zero of $\rho$ give a negligible dependency between the fields while large positive values give a strong positive correlation and large negative values give a strong negative correlation. However, a simple explicit relationship with the pointwise correlation coefficient does not generally exist. The effect on the pointwise correlation is highlighted in Fig. 1 showing a realization from such a bivariate Gaussian random field model. Here, both fields are stationary and anisotropic but with different directions of the main principal axes and different smoothness parameters. Even though $\rho = -0.98$, which would have corresponded to a correlation of $-0.7$ if the marginal random fields would have been equal in distribution, the actual correlation between the fields is lower since the two fields are not equal in distribution. It is however visible that peaks in the left field still tend to correspond to valleys in the right field, indicating a negative correlation.

## 3. Model discretization

To be able to use the model of the previous section in applications we must first discretize it. This is performed using a finite element approximation of the system of SPDEs. In this section we provide the details of this procedure. We first present the univariate case with $\alpha = 2$, then generalize to arbitrary $\alpha > 1$, and finally combine the methods for the multivariate setting.

### 3.1. The univariate case

In the case when $\alpha = 2$ in (1) the model can be discretized using a standard Galerkin finite element method as suggested by Lindgren et al. [18]. The aim is to approximate the solution $X$ by a basis expansion $X_h(\mathbf{s}) = \sum_{j=1}^N U_j \phi_j(\mathbf{s})$. Here $\{\phi_j\}_{j=1}^N$ is a set of piecewise linear functions induced by a triangular mesh of the spatial domain. Let $V_h$ be the space spanned by these basis functions. Augmenting the operator with homogeneous Dirichlet boundary conditions and considering the weak formulation of the SPDE on $V_h$ yields the following system of equations for the coefficients in the basis expansion,

$$\sum_{j=1}^N \left(\langle \tau\phi_j, \phi_i\rangle + \langle H\nabla\tau\phi_j, \nabla\left(\kappa^{-2}\phi_i\right)\rangle\right) U_j \overset{d}{=} \langle \kappa^{-1}\mathcal{W}, \phi_i\rangle, \quad i = 1, \ldots, N,$$

where $\langle\cdot,\cdot\rangle$ denotes the inner product on $\mathcal{G}$. This system of equations can be written in matrix form as $KU := (B + G)U \overset{d}{=} W$, where

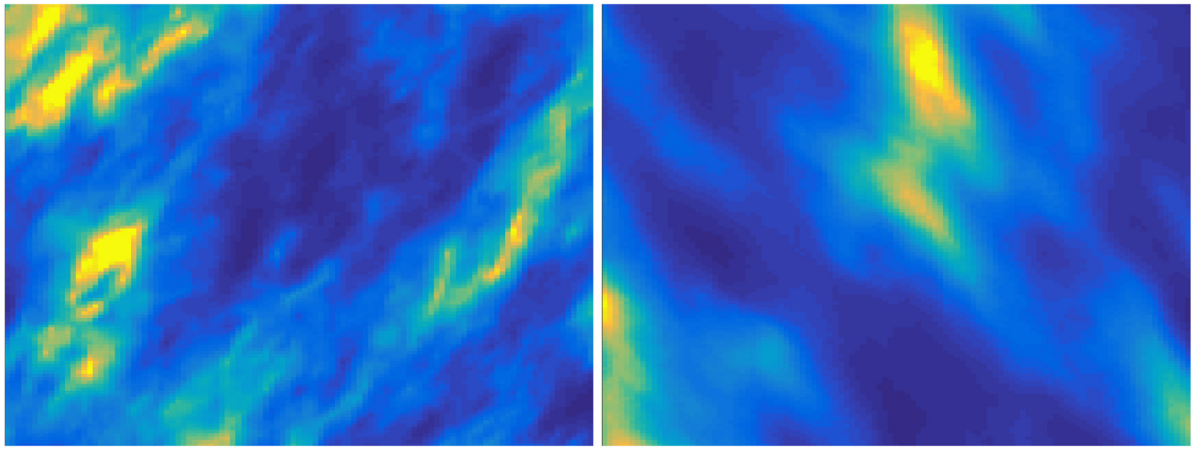

**Fig. 1.** Realization of a bivariate, anisotropic and stationary Gaussian random field. The left field has a correlation range of 25 in the direction of the principal axis at 45° and a correlation range of 14 in the perpendicular direction. The right field has the principal direction at an angle of −45° with the correlation range 30, the perpendicular direction has a range of 15. The correlation between the fields is controlled by $\rho = -0.98$. Furthermore, the left field has a smoothness constant of $\alpha = 1.6$ while the right field has $\alpha = 3$.

$B_{ij} := \langle \tau\phi_j, \phi_i\rangle$, $G_{ij} := \langle H\nabla\phi_j, \nabla\left(\kappa^{-2}\phi_i\right)\rangle$, and $W \sim \mathbb{N}(0, C)$ with $C_{ij} := \langle \kappa^{-2}\phi_j, \phi_i\rangle$. Hence, the stochastic weights of the basis expansion are $U \sim \mathbb{N}(0, K^{-1}CK^{-T})$.

The important property of using a basis of $V_h$ with compact support is that $K$ and $C$ will be sparse matrices. Lindgren et al. [18] showed that $C$ can be approximated by a diagonal matrix, with diagonal elements $\langle \phi_i, 1\rangle$. With this approximation, the precision matrix $KC^{-1}K$ is also sparse and $U$ is a Gaussian Markov random field (GMRF). This greatly reduces the computational cost for inference and simulation [24]. We refer to [17] for further details for the case of a univariate random field.

### 3.2. Rational approximation for arbitrary smoothness

The procedure from the previous subsection can be extended to even values of $\alpha$ by noting that the solution to $\kappa\mathcal{L}^2 X = \mathcal{W}$ can be obtained by first solving $\mathcal{L}X_1 = \kappa^{-1}\mathcal{W}$ and then $\mathcal{L}X = X_1$. One can therefore use the discretization from the previous subsection iteratively to obtain a discretization for even integer values of $\alpha$. Lindgren et al. [18] also stated the solution to $\mathcal{L}^{1/2}X = \mathcal{W}$ as a least square solution, which can be combined with the iterative procedure to obtain discretizations also for odd integer values of $\alpha$. This was utilized in [17] where only integer values of $\alpha$ were considered.

For large values of $\alpha$, the correlation function does not change much for a small change in $\alpha$. However, for small values of $\alpha$, restricting it to integer values constrain the flexibility of the model. For instance, the exponential correlation function corresponds to $\alpha = 1.5$ and cannot be modeled by an integer-valued $\alpha$. Therefore, in this work we want to model any well-defined smoothness value, i.e., $\alpha > d/2$ and not only integer values. Until recently it was not clear how to formulate a FEM approximation for non-integer valued $\alpha$. However, Bolin and Kirchner [25] solved this problem by combining the FEM approximation with a rational approximation $\frac{p_l(x)}{p_r(x)}$ of the power function, i.e., $x^{\alpha/2}$, where $p_l$ and $p_r$ are polynomials of some chosen orders. Specifically, $p_r(x) = \sum_{i=0}^{m} c_i x^{m-i}$ and $p_l(x) = \sum_{j=0}^{m+1} b_J x^{m+m_\alpha - J}$, where $m$ is an integer controlling the quality of the approximation, and $m_\alpha = \max\{1, \lfloor \alpha/2 \rfloor\}$. By using such a decomposition it was possible to approximate the non-integer power of a pseudo-differential operator $\mathcal{L}^{\alpha/2}$ as $p_l(\mathcal{L})p_r(\mathcal{L})^{-1}$. Substituting $\mathcal{L}^{\alpha/2}$ by $p_l(\mathcal{L})p_r(\mathcal{L})^{-1}$ in the equation $\mathcal{L}\,\mathrm{X} = \mathcal{W}$, one obtains

$$p_l(\mathcal{L})p_r(\mathcal{L})^{-1}\,\mathrm{X}_m^R = \mathcal{W},$$

where $\mathrm{X}_m^R$ is the rational approximation of X. The solution can be written as a system of equations,

$$\begin{aligned} p_l(\mathcal{L})Z &= \mathcal{W} \\ X_m^R &= p_r(\mathcal{L})Z. \end{aligned} \tag{3}$$

This is important since a FEM approximation of $p_l(\mathcal{L})Z = \mathcal{W}$ can be used in order to get a GMRF approximation of $Z$. More specifically, by computing the roots of the two polynomials, the discretized FEM operators $P_l$ and $P_r$ can be written as,

$$P_l := b_{m+1}K^{m_\alpha - 1}\prod_{j=1}^{m+1}\left(I - r_{l,j}K\right), \quad P_r := c_m\prod_{i=1}^{m}\left(I - r_{r,i}K\right),$$

where $K$ is the FEM matrix of Section 3.1. The coefficients $b_{m+1}, c_m$, $r_{l,j}, r_{r,i}$ are obtained from the rational approximation of the function $x^{\alpha/2}$ (see Bolin and Kirchner [25]). A larger $m$ yields a better approximation but also more terms in the polynomial operators, which will increase the computational cost by making $P_l$ and $P_r$ less sparse as well as decrease the numerical stability of the corresponding precision matrix.

The distribution of the stochastic weights is $U \sim \mathbb{N}(0, P_r P_l^{-1} C P_l^{-T} P_r^T)$. Even though both $P_r$ and $P_l$ are sparse, their inverses are not. Therefore, the precision matrix of $U$ will not be sparse either but because of the two-step procedure of the model formulation in Eq. (3), all computational benefits of the GMRF case can be maintained when using the model. This is accomplished by using the nested SPDE approach [26] and write $U = P_r\tilde{U}$, since $P_r$ is sparse and $\tilde{U}$ has a sparse precision matrix $P_l^T C^{-1} P_l$.

### 3.3. FEM for the bivariate model

We are now ready to discretize the model of (2). In the prior section we saw that we can write a rational FEM approximation of the operator $\mathcal{L}_X^{\alpha/2}$ as $K_X = P_l P_r^{-1}$. Likewise, denote the FEM approximation of the operator $\mathcal{L}_Y^{\beta/2}$ as $K_Y = Q_l Q_r^{-1}$. Moreover, we can consider $-\rho\kappa_Y\mathcal{L}_Y^{\beta/2}$ to be a composition of the three operators $-\rho\mathcal{I}$, $\kappa_Y\mathcal{I}$, and $\mathcal{L}_Y^{\beta/2}$. Likewise, $\sqrt{1+\rho^2}\kappa_X\mathcal{L}_X^{\alpha/2}$ as a composition of $\sqrt{1+\rho^2}\kappa_X\mathcal{I}$ and $\mathcal{L}_X^{\alpha/2}$. By considering an iterative FEM approximation with respect to these compositions we acquire the system of linear equations,

$$\begin{aligned} K_{\tilde{X}}U_X + K_\rho U_Y &= W \\ K_{\tilde{Y}}U_Y &= V, \end{aligned}$$

where $W$ and $V$ are i.i.d. $\mathbb{N}(0, C)$ random vectors and $U_X$ and $U_Y$ are the stochastic weights for the FEM approximation of $X$ and $Y$ respectively. Furthermore, $K_{\tilde{X}} = C^{-1}C_X K_X$ where $C_X = \{\langle\sqrt{1+\rho^2(\boldsymbol{s})}\kappa_X(\boldsymbol{s})\phi_i(\boldsymbol{s}), \phi_j(\boldsymbol{s})\rangle\}_{ij}$. This derives from the FEM approximation of the operator $\sqrt{1+\rho^2(\boldsymbol{s})}\kappa_X(\boldsymbol{s})$. Likewise, $K_{\tilde{Y}} = C^{-1}C_Y K_Y$ where $C_Y = \{\langle\kappa_Y(\boldsymbol{s})\phi_i(\boldsymbol{s}), \phi_j(\boldsymbol{s})\rangle\}_{ij}$, and $K_\rho = -C^{-1}C_\rho K_{\tilde{Y}}$ where $C_\rho = \{\langle\rho(\boldsymbol{s})\phi_i(\boldsymbol{s}), \phi_j(\boldsymbol{s})\rangle\}_{ij}$. The reason for dividing the operators into compositions that are estimated by iterative FEM are due to $K_X$ and $K_Y$ being FEM approximations

$$\tilde{Q} = \begin{bmatrix} P_l^T \left(C_X^T C^{-3} C_X\right) P_l & -P_l^T \left(C_X^T C^{-3} C_\rho C^{-1} C_Y\right) Q_l \\ -Q_l^T \left(C_Y^T C^{-1} C_\rho^T C^{-3} C_X\right) P_l & Q_l^T \left(C_Y^T C^{-3} C_Y + C_\rho^T C^{-1} C_Y^T C^{-3} C_Y C^{-1} C_\rho\right) Q_l \end{bmatrix}. \tag{4}$$

**Box I.**

of the pseudo-differential operators. As such it would be problematic to include the spatially varying parameters, $\kappa_X, \kappa_Y$, and $\rho$ into these matrices since they would also be affected by a differential operator.

The block covariance matrix for $U_X$ and $U_Y$ becomes,

$$\begin{bmatrix} \sigma_X & \sigma_{XY} \\ \sigma_{YX} & \sigma_Y \end{bmatrix} = \begin{bmatrix} K_{\tilde{X}}^{-1} C K_{\tilde{X}}^{-T} + K_{\tilde{X}}^{-1} K_\rho K_{\tilde{Y}}^{-1} C K_{\tilde{Y}}^{-T} K_\rho^T K_{\tilde{X}}^{-T} & -K_{\tilde{X}}^{-1} K_\rho K_{\tilde{Y}}^{-1} C K_{\tilde{Y}}^{-T} \\ -K_{\tilde{Y}}^{-1} C K_{\tilde{Y}}^{-T} K_\rho^T K_{\tilde{X}}^{-T} & K_{\tilde{Y}}^{-1} C K_{\tilde{Y}}^{-T} \end{bmatrix}.$$

The corresponding block precision matrix is,

$$\begin{bmatrix} q_X & q_{XY} \\ q_{YX} & q_Y \end{bmatrix} = \begin{bmatrix} K_{\tilde{X}}^T C^{-1} K_{\tilde{X}} & K_{\tilde{X}}^T C^{-1} K_\rho \\ K_\rho^T C^{-1} K_{\tilde{X}} & K_{\tilde{Y}}^T C^{-1} K_{\tilde{Y}} + K_\rho^T C^{-1} K_\rho \end{bmatrix}.$$

Note that this is not the sparse matrix needed to acquire the important computational advantages of the SPDE approach. However, by using the idea introduced in the previous section, we can formulate the model as a nested model and keep the computational benefits of a Gaussian Markov random field. This is done by considering $U_X = P_r \tilde{U}_X$ and $U_Y = Q_r \tilde{U}_Y$ where $\left[\tilde{U}_X, \tilde{U}_Y\right] \sim \mathbb{N}\left(\mathbf{0}, \tilde{Q}\right)$ becomes a GMRF with Eq. (4) as given in Box I.

In the last step, the fact that $C$ is symmetric was used.

In reality, the precision matrix of Eq. (4) is not Markov since $C^{-1}$ is not sparse. However $C$ can be approximated by a diagonal matrix with diagonal elements $\{\langle \phi_i, 1 \rangle\}_i$. This procedure is known as mass lumping and is a necessary approximation for acquiring the important properties of the original SPDE-approach Lindgren et al. [18], and hence also necessary for our method. When assuming that $C$ is mass lumped, $\tilde{Q}$ is sparse and $C^{-1}$ can be computed easily from $C$. Also, it should be noted that the matrices $C_X, C_Y$, and $C_\rho$ likewise can be mass lumped. This is not required but highly beneficial since that yields a sparser $\tilde{Q}$; and will in general reduce approximation errors rather than enhancing them. With this formulation of the joint model the method of Bolin and Kirchner [25] can be used directly to acquire a computationally efficient model of arbitrary positive smoothness, $\alpha > d/2$.

For this work, this bivariate model was implemented in Matlab [27]. Most of the functionality of that implementation is also available in the free-to-use Python package Fieldosophy [28].

## 4. Data

In order to test the proposed model we will fit it to data from the ERA-Interim global atmospheric reanalysis [29] from the European Centre for Medium-Range Weather Forecasts (ECMWF). The reanalysis data is based on measurements and interpolated to a lattice grid in a longitude–latitude projection using ECMWFs weather forecasting model IFS, cycle 31r2 [30]. The spatial resolution of the data is 0.75° and it is available from 1979 to present. We will use the variables *significant wave height of wind and ground swells* and *mean wave period* from the dataset as $H_s$ and $T_1$ in our analysis. Both variables are available at a temporal resolution of 6 h. However, since we will not model the temporal evolution of the data, and therefore want to approximate data from different points in time as independent, we thin the data to a temporal resolution of 24 h. Data from different months are distributed differently due to the effects of the annual cycle. Because of this, one has to fit a model to each month (or at least each season) separately. Since it will be too complex to show results from all 12 months we from now on focus on the month of April. For April we use data from each day during the years 1979 to 2018. We also restrict the analysis spatially to the north Atlantic, since this region contains several important trading routes and is known to produce data that is approximately log-Gaussian distributed [4].

An example of two simultaneous observations of $H_s$ and $T_1$ from the data can be seen in Fig. 2. A bivariate histogram as well as marginal normal distribution plots of $\log H_s$ and $\log T_1$ for one specific point in space (−32.25° longitude and 48.75° latitude) are shown in Fig. 3. The data at this point agrees well with the assumption of a bivariate log-normal distribution and similar results are obtained for other locations in the spatial domain.

Fig. 4 shows normal probability plots of $\log H_s$ and $\log T_1$ for all points in the region. The data were first standardized, pointwise, before computing the plot.

The sample mean and sample variance of the logarithmized data are shown in Fig. 5. Clearly the mean wave height is decreasing close to the coasts while the variance is increasing slightly. The mean wave period, and to some extent the mean significant wave height, is larger to the east than to the west. This is caused by the mean wind direction being eastwards for most parts of the north Atlantic ocean.

The left columns of Figs. 7 and 8 show the empirical correlation between three reference points in space and every other point in the spatial domain. Apparently, the point close to the coast of USA is showing an anisotropic pattern with the principal axis on the diagonal. Contrary to this, the spatial correlation of the mid Atlantic and at the coast of northern Europe has the principal axis in the east–west direction. It should be noted that the data is portrayed in the longitude–latitude coordinate system in Figs. 7 and 8. Other projections would yield different shapes of anisotropy—however, it is clear that no stationary model (on the sphere or in a plane of any of the popular projections) can explain the observed behavior.

The considered dataset consists of 1200 days of data. We divide these into two equally-sized subsets of training data and test data. The training set consists of every second day starting from the first day available. The test set consists of the remaining days. Hence, the test- and training sets form a partition of all available days, each set consists of 600 days, at least 2 days apart. In the next section we will use the training set to estimate model parameters. The test set is used to compare the fitted model with data for the purpose of model validation.

## 5. Parameter estimation and model fit

Following Hildeman et al. [17], we logarithmize and standardize the data first, marginally pointwise using sample mean and sample variances from the training set. The standardized data is then modeled by the proposed mean-zero bivariate Gaussian random field ($\tau$ is fixed to a value corresponding to unit marginal variances due to the prior standardization). As is common in geostatistical models, we allow for a nugget effect for each dimension while estimating the model. That is, for a location $\mathbf{s}_i$, we assume that the observed values, $X_{obs,i}, Y_{obs,i}$, are $X_{obs,i} = X(\mathbf{s}_i) + \varepsilon_{X,i}$ and $Y_{obs,i} = Y(\mathbf{s}_i) + \varepsilon_{Y,i}$, where $\varepsilon_{X,i} \sim \mathbb{N}(0, \sigma_{X,e}^2)$ and $\varepsilon_{Y,i} \sim \mathbb{N}(0, \sigma_{Y,e}^2)$ are independent variables representing measurement noise. The nugget effect can also explain deviations between observed values on the same triangles of the FEM mesh, since our FEM implementation implicitly assumes a linear relationship between such observations.

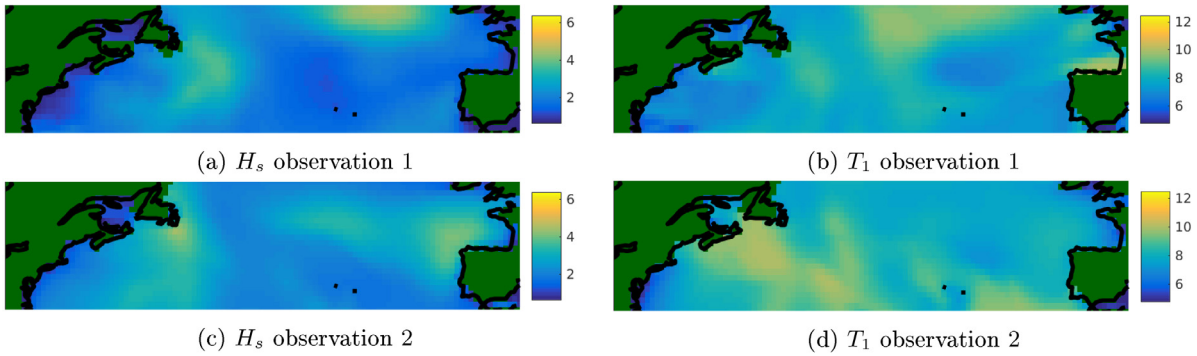


(a) $H_s$ observation 1 (b) $T_1$ observation 1

(c) $H_s$ observation 2 (d) $T_1$ observation 2

**Fig. 2.** Two observations of $H_s$ and $T_1$ chosen randomly from the dataset of April month during the years 1979–2018.

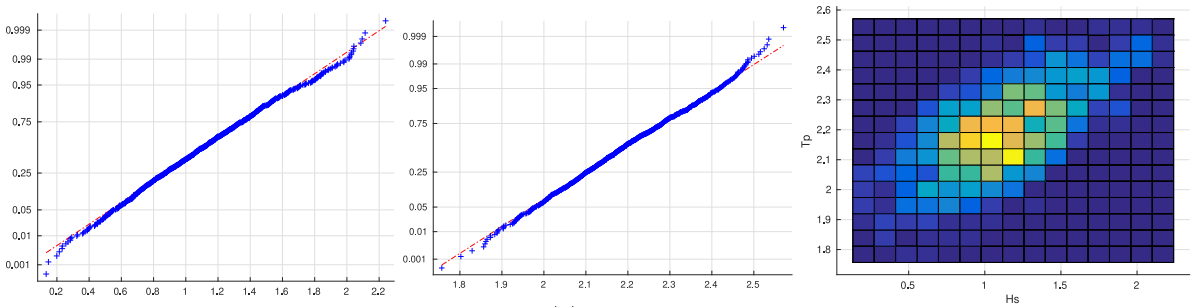


(a) $\log H_s$ (b) $\log T_1$ (c) Bivariate histogram

**Fig. 3.** Normal probability plots of the marginal distribution of $\log H_s$ and $\log T_1$ as well as their corresponding two dimensional histogram. The data is taken from a point at latitude 48.75° and longitude −35.25° from the ERA-Interim dataset.

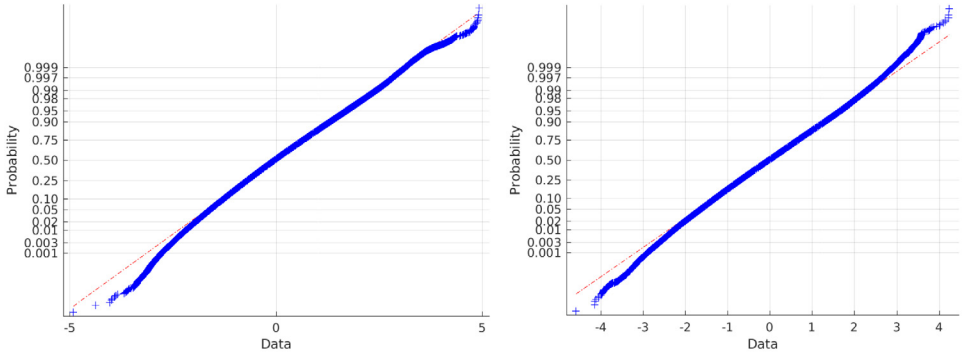


(a) $\log H_s$ (b) $\log T_1$

**Fig. 4.** Normal probability plots of all data, standardized for each spatial location separately.

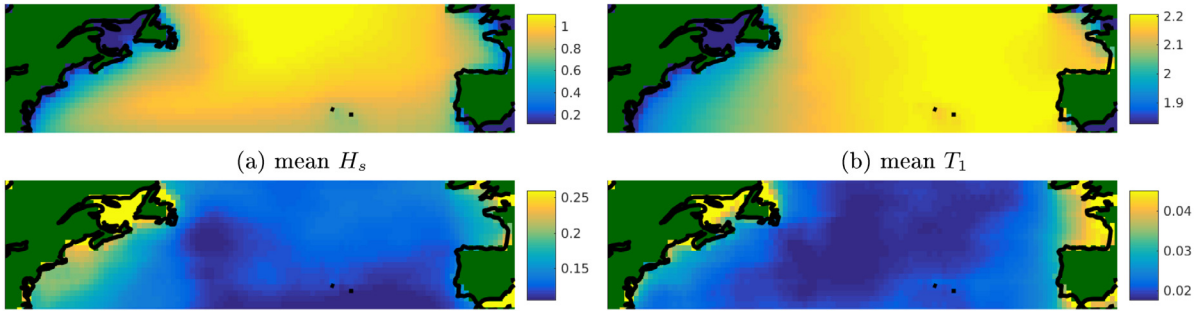


(a) mean $H_s$ (b) mean $T_1$

(c) variance $H_s$ (d) variance $T_1$

**Fig. 5.** Sample mean and sample variance for $H_s$ and $T_1$ in the north Atlantic.

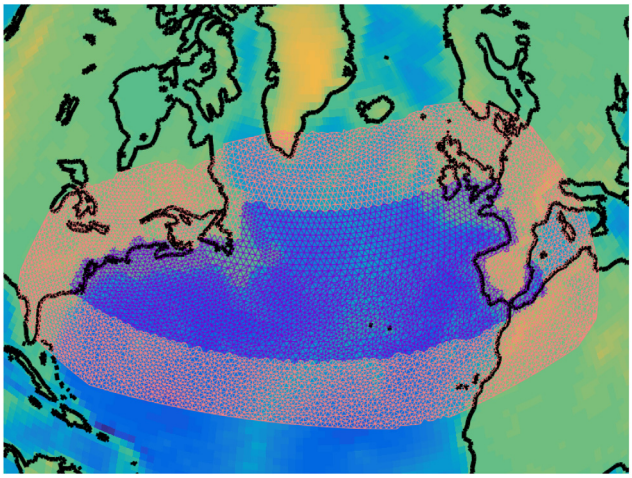

**Fig. 6.** The north Atlantic with the FEM mesh overlaid. Blue triangles are part of the spatial domain, $\mathcal{G}$. Pink triangles are part of the mesh extension. (For interpretation of the references to color in this figure legend, the reader is referred to the web version of this article.)

In order to use the proposed FEM model a triangular mesh has to be created over the spatial domain, $\mathcal{G}$. Since the spatial domain is in reality a subset of the surface of the globe—we create a mesh approximating $\mathcal{G}$ by a polyhedra, i.e., as a piecewise-planar manifold approximating the sphere. Hence, the region inside each triangle is planar but the triangles will not all be part of the same plane. Fig. 6 show the mesh created for the north Atlantic. The blue triangles correspond to triangles within $\mathcal{G}$ and the pink triangles make up the mesh extension used to remove boundary effects. As in Hildeman et al. [17], the barrier method [31] is used to reduce the required size of the mesh extension. Both SPDEs was equipped with homogeneous Dirichlet boundary conditions, although the chosen boundary conditions will not matter due to the mesh extension [18,17].

Since the parameters of the proposed model are not known a priori they have to be estimated from data. The proposed bivariate model is defined by the marginal random fields through $K_X$ and $K_Y$, and the cross-correlation function $\rho(\boldsymbol{s})$. The likelihood function of the joint model can be computed explicitly with a computational cost of $\mathcal{O}(N^{3/2})$, where $N$ are the number of nodes in the triangular mesh. The maximum likelihood (ML) estimates of the parameters cannot be computed explicitly, instead numerical optimization using a quasi-Newton algorithm is used to acquire the parameter estimates. Furthermore, the initial values of the optimization algorithm is chosen using local parameter estimates as proposed in [17].

Although the joint likelihood can be optimized numerically we propose a stepwise parameter estimation procedure where we fit $X$ and $Y$ independently in a first step. Then, conditioned on the estimates of the univariate random field parameters, a ML estimate of the cross-correlation structure, $\rho(\boldsymbol{s})$, is computed. The motivation for this procedure is as follows:

One of the strengths of the proposed model is that all parameters have intuitive interpretations. The parameters of $K_X$ and $K_Y$ respectively explain the spatial distribution of the random fields $X$ and $Y$ independently of each other. Since the real spatial cross-correlation structure between $X$ and $Y$ likely is too complex to be explained completely by just $\rho(\boldsymbol{s})$, some degree of model-misspecification will be present. Maximizing the full likelihood function corresponds, asymptotically, to minimizing the Kullback–Liebler divergence between the true data distribution and the assumed model. However, under model-misspecification, full ML estimates of the bivariate fields do not necessarily estimate the parameters of the original interpretation; instead, the estimates will correspond to the values that are minimizing the distance between the true model and the proposed one. This is not a desirable feature in many applications—especially if conclusions should be drawn based on the estimated values of the parameters themselves.

Estimating the parameters of $K_X$ and $K_Y$ independently has the additional advantage that it allows a lower dimensionality in the quasi-Newton optimization; which reduces the computational cost of estimation as well as decreases the risk of finding bad local optima. Also, the parameters of $K_X$ and $K_Y$ independently can be computed in parallel, further reducing the wall clock time of the parameter estimation procedure.

### 5.1. Estimation of the univariate random fields

The models for $X$ and $Y$ independently are parametrized by the smoothness $\alpha$, the nugget effect, as well as the functions $H(\boldsymbol{s})$ and $\kappa(\boldsymbol{s})$. As in Hildeman et al. [17], we define

$$\tilde{H}(\boldsymbol{s}) = \begin{bmatrix} \exp\left(h_1(\boldsymbol{s})\right) & \left(2S(h_3(\boldsymbol{s}))-1\right)\exp\left(\frac{h_1(\boldsymbol{s})+h_2(\boldsymbol{s})}{2}\right) \\ \left(2S(h_3(\boldsymbol{s}))-1\right)\exp\left(\frac{h_1(\boldsymbol{s})+h_2(\boldsymbol{s})}{2}\right) & \exp\left(h_2(\boldsymbol{s})\right) \end{bmatrix},$$

and let $\kappa(\boldsymbol{s}) = \left|\tilde{H}(\boldsymbol{s})\right|^{-1/2}$, and $H(\boldsymbol{s}) = \kappa(\boldsymbol{s})^2\tilde{H}$. The functions $h_1, h_2, h_3$ are defined as low-dimensional regressions on cosine functions over the domain of interest,

$$h_i(\boldsymbol{s}) = \sum_{p=0}^{k}\sum_{n=0}^{k}\beta_{np}^{i}\cos\left(n\frac{\pi s_1}{S_1}\right)\cos\left(p\frac{\pi s_2}{S_2}\right), \quad i = 1,2,3, \tag{5}$$

where $\boldsymbol{s} = (s_1, s_2)$ and $S_1, S_2$ denotes the width and height of the bounding box of the locations of observations. The advantage of this parameterization is that we do not have any restrictions on the coefficients $\beta_{np}^{i}$ in order to obtain a valid model. We use $k = 4$ in Eq. (5), meaning that $25 \cdot 3 + 2 = 77$ parameters were estimated simultaneously using the quasi-Newton method for each field.

The estimated correlation functions for three reference points are visualized in Figs. 7 and 8. Thus, the figures show the correlation between the reference points and all other points in the domain. These three reference points have the coordinates 296° longitude, 37° latitude (close to the east coast of USA), 320° longitude, 44° latitude (in the middle of the north Atlantic), and 342° longitude, 51° latitude (close to the west coast of Ireland). The figures suggests that the correlation structures are quite similar between $\log H_s$ and $\log T_1$, which makes sense since they are positively correlated.

The estimated smoothness parameter of $\log H_s$ was $\alpha = 3.66$, corresponding to a random field which is almost surely two times mean-square differentiable. In Hildeman et al. [17] the same model was fitted to $\log H_s$ with the difference that it was defined in the longitude–latitude projection instead of on the sphere and that the smoothness parameter could only be integer-valued. In that work the smoothness was found to be $\alpha = 3$. Likewise, the estimated smoothness of $\log T_1$ was $\alpha = 3.16$. Hence, the wave period is spatially a little bit rougher compared to the significant wave height.

### 5.2. Estimation of the cross-correlation structure by ML

Given the marginal parameters of $X$ and $Y$ we now want to estimate their cross-correlation structure, i.e., $\rho(\boldsymbol{s})$. We parametrize this function as a regression on cosines as in (5). As a first attempt of estimating $\rho(\boldsymbol{s})$, we use ML conditioned on the already estimated parameters for $X$ and $Y$. Fig. 9 compares the estimated cross-correlation structure with the empirical one estimated from data. The reference point used in this figure was at 320° longitude and 44° latitude.

Surprisingly, even though the data is strongly positively correlated, the fitted model yielded a strong negative correlation. It turns out that the proposed model of the cross-correlation structure is a bit too simplistic to explain the true dependency between $\log H_s$ and $\log T_1$. The reason being that the point, $\boldsymbol{s}_2$, where $\log T_1$ has the strongest cross-correlation with $\log H_s(\boldsymbol{s}_1)$ is not $\boldsymbol{s}_1$. However, this is assumed in the

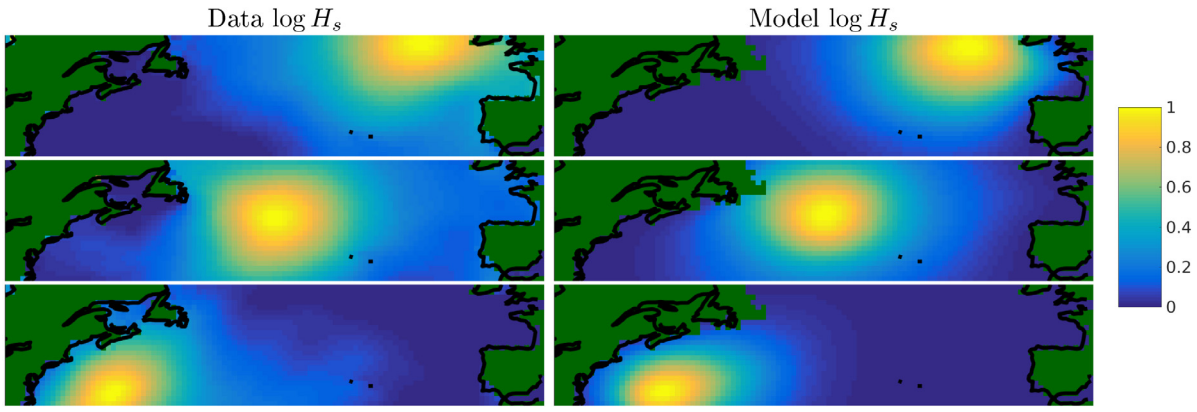


**Fig. 7.** Correlation between three different reference points and all other points in $\log H_s$. Left column: empirical correlation function from data. Right column: correlation function from fitted model.

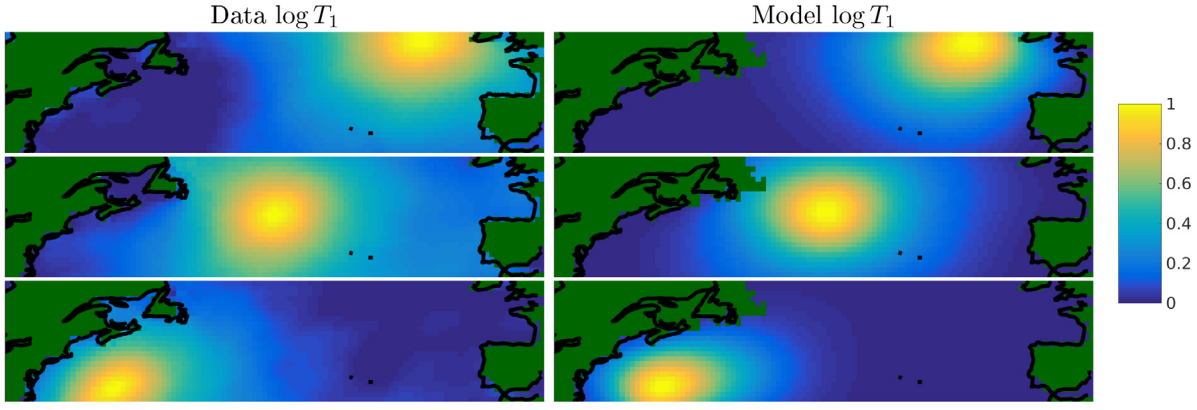


**Fig. 8.** Correlation between three different reference points and all other points in $\log T_1$. Left column: empirical correlation function from data. Right column: correlation function from fitted model.

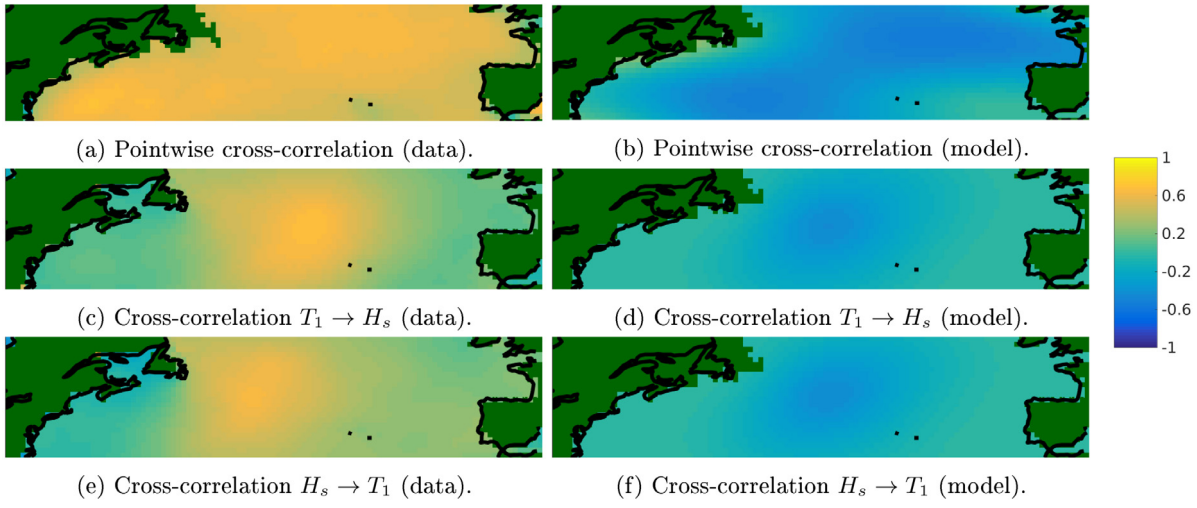


**Fig. 9.** Cross-correlation from joint maximum likelihood estimation of cross-correlation structure. Top row: comparison of, pointwise cross-correlation between the data and the estimated model. Middle row: comparison of cross-correlation between $\log T_1$ at a reference point and $\log H_s$ for all points in $\mathcal{G}$. Bottom row: comparison of cross-correlation between $\log H_s$ at a reference point and $\log T_1$ for all points in $\mathcal{G}$.

proposed model of Section 2. For the reference point at 320° longitude and 44° latitude the translation between the reference point and the point of maximum cross-correlation can be seen in Fig. 10. Considering the value of $\log H_s$ in the reference point the corresponding $\log T_1$ is generally further west, while the opposite relationship holds for $\log T_1$ in the reference point. Corresponding vectors between reference points in $\log H_s$ and maximum points of correlation with $\log T_1$ can also be seen in Fig. 10.

Fig. 11 shows the ratio between the points of highest cross-correlation and the pointwise cross-correlation. For most regions, the pointwise cross-correlation is not that much smaller than the maximum cross-correlation. However, since there is a clear consistent

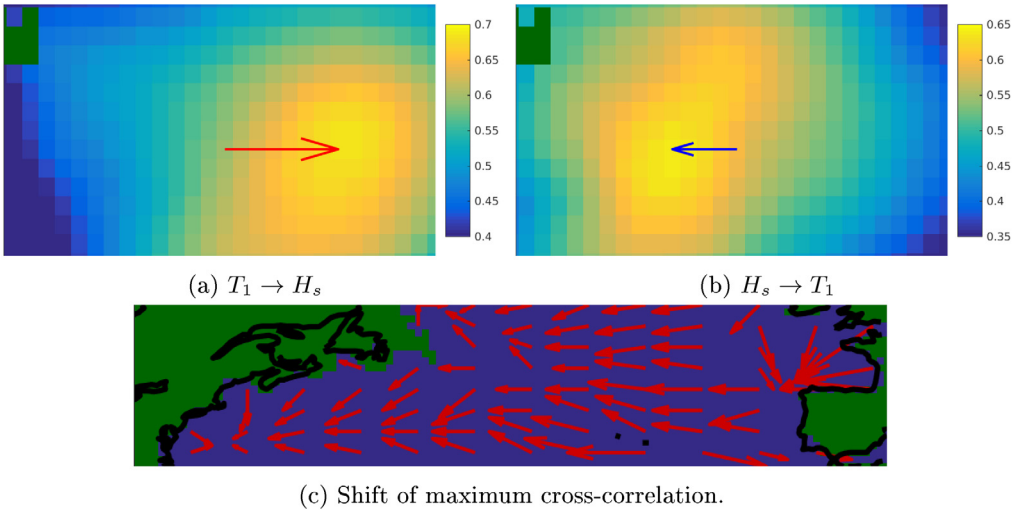


**Fig. 10.** Top row: translation vectors between a reference point $s_r$ at (320°, 44°) and its maximum cross-correlation value (estimated from data). Cross-correlation between $\log T_1(s_r)$ and $\log H_s(s)$ for $s$ close to $s_r$ (left) and cross-correlation between $\log H_s(s_r)$ and $\log T_1(s)$ (right). Bottom row: translation vectors between $H_s$ and corresponding maximum cross-correlation with $T_1$ for several points in the domain.

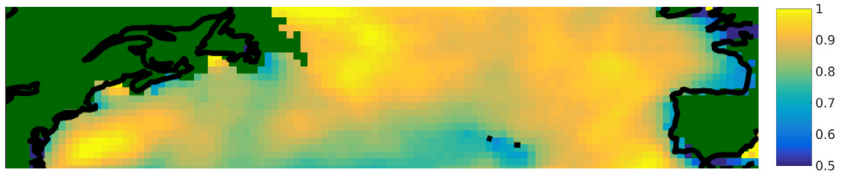


**Fig. 11.** Ratio between maximum cross-correlation and pointwise cross-correlation for all points in the spatial domain.

increase in cross-correlation when moving away from the reference point the maximum likelihood estimate of $\rho$ is negative. This obvious model-misspecification is another reason for using the proposed stepwise estimation procedure.

These results suggest that the bivariate model will not explain the joint distribution perfectly. However, it can still be useful if one could obtain a better method of estimating $\rho$. Let us therefore propose such a method.

### 5.3. Estimation of the cross-correlation structure by pointwise ML

Instead of estimating $\rho$ by ML a possible solution is to fit the model to explain the pointwise cross-correlation, instead of the total cross-correlation. This corresponds to maximizing a product likelihood of the bivariate Gaussian random variables for each spatial location, i.e., the log-likelihood function,

$$l(\rho; \boldsymbol{x}, \boldsymbol{y}) = l(\rho; \hat{\boldsymbol{\gamma}}) = \sum_{j=1}^{M} O_j \left[ -\log(2\pi) - \frac{1}{2}\log\left(1-\gamma_j^2\right) + \frac{\gamma_j}{1-\gamma_j^2}\left(\frac{O_j-1}{O_j}\hat{\gamma}_j\right)\right].$$

Here, $M$ is the number of spatial locations in the data, $O_j$ are the number of observations for location $j$, and $\gamma_j$ is the pointwise cross-correlation between the two fields at location $\boldsymbol{s}_j$ according to the model. The observations, $\boldsymbol{x} := \{x_{jk}\}_{j,k}$ and $\boldsymbol{y} := \{y_{jk}\}_{j,k}$ are not needed explicitly since the sample pointwise cross-correlations, $\hat{\boldsymbol{\gamma}}$, are sufficient statistics for evaluating the log-likelihood. The pointwise cross-correlations of the model are $\boldsymbol{\gamma} = A_j . P_r \tilde{\Sigma}_{XY} Q_r^T A_j^T$, where $A$ is the $M \times N$ observation matrix, mapping the nodal values of the FEM approximation to values at the observation locations [18]. The matrix $\tilde{\Sigma}_{XY}$ is the $N \times N$ off-diagonal block of $\tilde{\Sigma}$ which is the covariance matrix of $[\tilde{U}_X, \tilde{U}_Y]$, as defined in Section 2 together with $P_r$ and $Q_r$. To reduce the computational cost of computing $\Sigma_j$, we use the Takahashi equations [32,33] to compute the needed elements of $\tilde{\Sigma}$ based on the corresponding precision matrix—without computing the full inverse which is non-sparse.

When we estimate the parameters, the pointwise sample cross-correlations $\{\hat{\gamma}_j\}_j$ are replaced with the sample cross-correlations between $H_s$ at location $\boldsymbol{s}_j$ and $T$ at the location which maximized the pointwise cross-correlation. In this way the fitted model will have a pointwise cross-correlation corresponding to the maximum cross-correlation of that point—instead of fitting a true pointwise cross-correlation that will underestimate the maximum cross-correlation somewhat.

To get an understanding of the true cross-correlation structure of the estimated parameters Figs. 12 and 13 show the cross-correlation between the three reference points in one of the fields and all points in the other field. Finally, Fig. 14 shows realizations from the final model, which look similar to the observed data in Fig. 2.

## 6. Applications

In this section we look into two applications in maritime safety for which information about both $H_s$ and $T$ are used. One is an extension of the fatigue damage application considered in Hildeman et al. [17]. The other is a method of estimating the risk of capsizing due to a specific capsizing mode known as *broaching-to*.

### 6.1. Accumulated fatigue damage

A ship traversing the ocean is subjected to wear due to wave encounters. These encounters will create microscopic cracks in the hull of the ship. With time and further exposure to the wave environment such cracks will grow while new will form. This type of wear damage is called fatigue. A ship will accumulate a certain amount of fatigue damage on any journey. However, the accumulated fatigue damage will vary in severity depending on the sea states encountered en route. Mao et al. [34] proposed the following formula based on $H_s$ and $T_z$ for

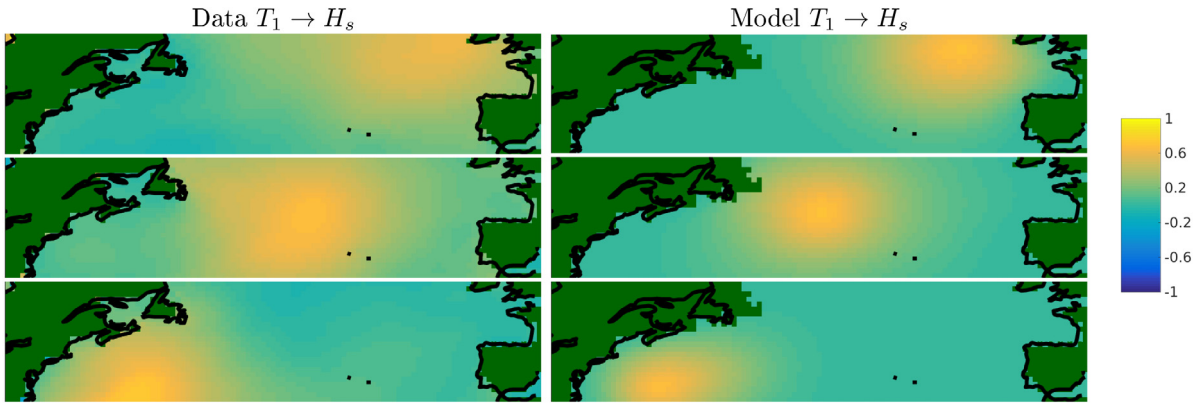


**Fig. 12.** Cross-correlation between three reference points in $\log T_1$ and all other points in $\log H_s$. Left column: empirical cross-correlation function from data. Right column: cross-correlation function from fitted model using pointwise ML estimates.

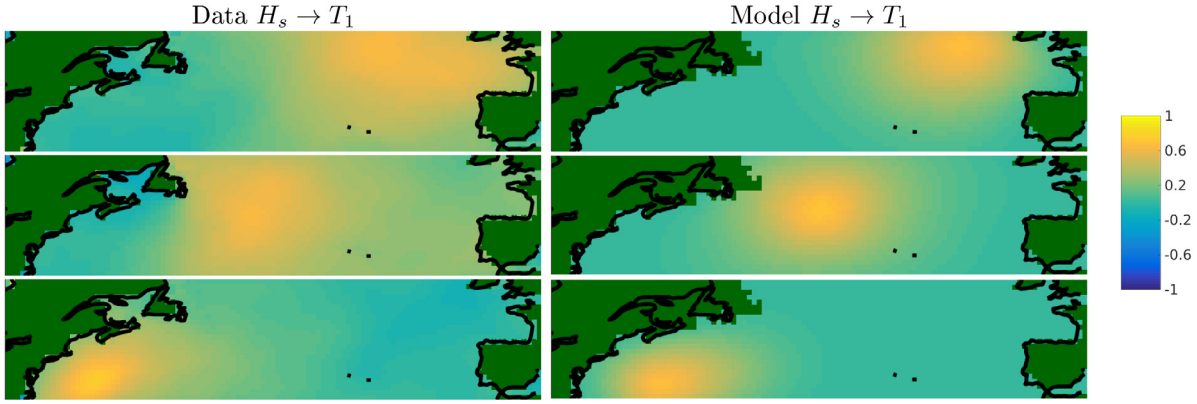


**Fig. 13.** Cross-correlation between three reference points in $\log H_s$ and all other points in $\log T_1$. Left column: empirical cross-correlation function from data. Right column: cross-correlation function from fitted model using pointwise ML estimates.

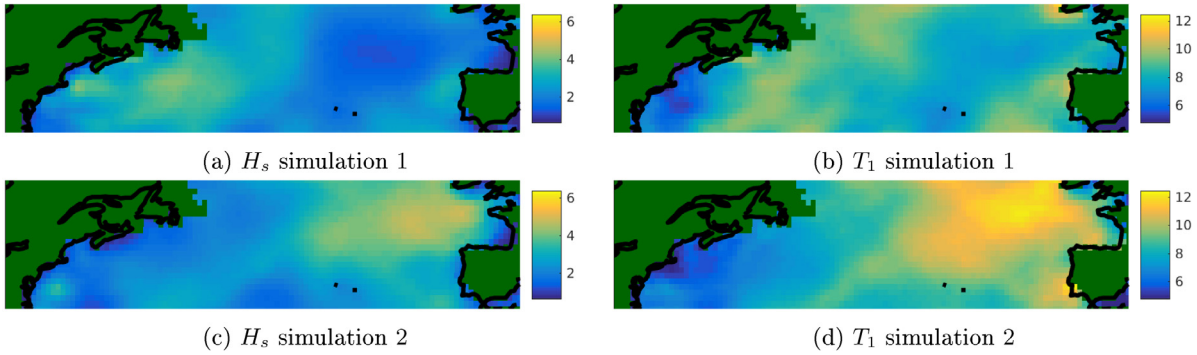


**Fig. 14.** Two simulations of $H_s$ and $T_1$ from the joint spatial model.

which the expected rate, $d(t)$, of accumulated fatigue damage could be computed,

$$d(t) \approx \frac{0.47 C^{\beta} H_s^{\beta}(\boldsymbol{s}(t))}{\gamma} \left( \frac{1}{T_z(\boldsymbol{s}(t))} - \frac{2\pi V(t) \cos \phi(t)}{g T_z^2(\boldsymbol{s}(t))} \right). \tag{6}$$

Here, $g$ is the gravitational constant ($\approx 9.81$), $V$ is the speed of the ship, and $\phi$ is the angle between the heading of the ship and the direction of the traveling waves. Further, $\gamma$ and $\beta$ are constants dependent on the material of the ship and $C$ is a constant depending on the ship's design [34]. This formula can be used in combination with Monte Carlo simulations based on $H_s$ and $T_z$ from our proposed model to evaluate the distribution of accumulated fatigue damage on a planned route.

We consider the transatlantic route of Fig. 15(a). The continuous route is approximated by line segments between 100 evenly spaced locations (in geodesic distance) between the start and end points of the route. We set the ship speed to a fixed value of 10 [m/s] which yields a sailing duration of 149.69 h or equivalently 6.23 days. The heading of the ship, in one of the 100 locations on the route, is approximated as the mean between the direction acquired from the two connecting line segments. We consider the journey to take place in April, since we have estimated the parameters of the model for this month. A ship traversing the considered route can be modeled by a curve in space and time, $\boldsymbol{s}_\gamma(t)$. Since we have neither a spatio-temporal model nor data with sufficient temporal resolution we consider the sea states to remain constant in time during the traversal of the route. We denote the accumulated fatigue damage during the trip up until time $t$ as $D(t)$, where $t = 0$ corresponds to the start of the trip with no accumulated damage and $t = t_{end}$ corresponds to the end of the

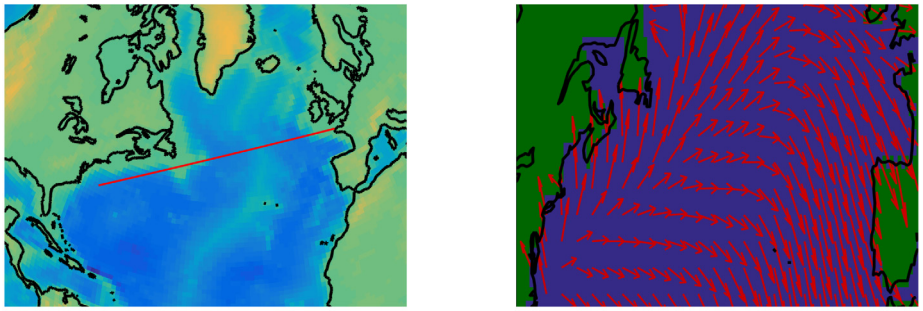

(a) Transatlantic route of ship. (b) Mean wave directions during April.

**Fig. 15.** Route of ship and the mean wave directions during month of April.

trip with the most accumulated damage. We set the constants specific to the ship as in [35,34,17], i.e., $C = 20, \beta = 3$, and $\gamma = 10^{12.73}$. In order to compute the fatigue we also need the propagating waves angle in comparison with the ships heading. This is a random quantity that is not modeled in this work. Instead we assume that the mean direction of the wave propagation is the same as the direction that the contour lines of $H_s$ moves, i.e. the direction of the gradient of $H_s$ field (this is the same wave direction as used in [35,34,17], which has shown good results). This direction was estimated in Baxevani and Rychlik [36] and can be seen in Fig. 15(b). Furthermore, assuming that the sea states can be characterized by Bretschenider spectrums, $T_z = \frac{1.2965}{1.408} T_1 = 0.9208 \cdot T_1$. With these assumptions, and given values of $H_s$ and $T_1$, we use (6) to compute the corresponding values of $d(t)$ and approximate the accumulated fatigue damage as

$$D(T) = \int_0^{t_{end}} d(t)dt \approx \sum_{i=1}^{100} d(t_i)\Delta t,$$

where $\Delta t$ is the time differences between the 100 consecutive point locations on the considered route, $\Delta t = 1.4969$ h.

The accumulated fatigue damage is computed for each of the 600 days available in the test set of the data. Hence, we acquire a sample of 600 values of accumulated fatigue damage. Fig. 16 shows the empirical CDF computed from this sample (blue line). The accumulated damage is computed for a ship traversing the route in both directions, since the accumulated damage will depend on the angle between the heading of the ship and the propagation direction of the waves it will yield a different result depending on the direction of the route.

In order to assess whether the estimated CDF from data behaves as if estimated from the model we also estimate 200 CDFs from independent sets of "fake" data generated from the model. That is, we generate 600 independent realizations of the bivariate $H_s, T_z$ surface and compute an empirical CDF. This is then repeated 200 times. In Fig. 16 these 200 estimated CDFs are plotted (green lines) together with the pointwise upper and lower envelopes of the values (red lines). As can be seen, the estimated CDF from data is within the envelopes, suggesting that the true data and the model cannot be distinguished using fatigue damage predictions.

In Hildeman et al. [17], a similar comparison was performed where the accumulated fatigue damage was computed using only $H_s$. Instead of $T_z$ the proxy $T_z = 3.75\sqrt{H_s}$ was used, as proposed in [34,35]. Hildeman et al. [17] showed that the accumulated fatigue damage of the model agreed well with observed data. However, in that work only data of $H_s$ was available. Hence, the data that the model was compared to also used the proxy $T_z = 3.75\sqrt{H_s}$. Since we now have data of both $H_s$ and $T_z$ we can compare this proxy with data from the real bivariate random field. Fig. 17 shows the corresponding CDFs and one can note that the use of the proxy does not provide accurate estimates of the true distribution of fatigue damage. In the direction from America to Europe the model underestimates the damage while in the other direction it overestimates it. This suggests that it is necessary to use a bivariate model in order to model accumulated fatigue damage correctly.

However, instead of using the full bivariate model another possible simpler alternative is to model $T$ as the pointwise conditional mean given $H_s$. In such a model only $H_s$ has to be modeled spatially. Compared to the proxy model of Hildeman et al. [17] the pointwise cross-correlation between $H_s$ and $T_z$ would still need to be estimated. Using this conditional means model for $T_z$ given $H_s$ yields the estimated CDFs as in Fig. 18. Also this simpler model seemed sufficient to explain the distribution of fatigue damage accumulated on the transatlantic route.

### 6.2. Safety of operation in a following sea

Although a capsizing is rare it is important to minimize the risk of such an event occurring. Measures to avoid capsizing should be undertaken both in naval architecture of hull designs of new vessels and for operational recommendations. A natural approach to capsize modeling is to view it as an extremal problem to be handled by the machinery of extreme value theory. However, efforts to do this by fitting specific extreme value distributions, e.g., to maximum roll angle values, have not been overly successful. The variety of capsize modes suggests that a variety of modeling approaches may be required. In this section the so called broaching-to capsize mode will be analyzed using the method proposed in [37]. The goal is to see if the proposed bivariate model can be used for modeling risks of broaching-to.

For a vessel sailing in a following sea a large overtaking wave may trigger a response which may put the vessel in a dangerous situation and potentially lead to a capsizing. There are several ways such an event may develop. One of these, referred to as *broaching-to*, happens when an overtaking wave forces a quick and uncontrolled yaw. This might place the ship in beam sea or worse, the quick turn might create a centrifugal moment leading to a large heel angle, displacement of load with following listing, and/or possibly capsizing [38]. In moderate sea states a vessel is likely to broach-to if it runs with high speed and is slowly overtaken by steep and relatively long waves. However, it may also occur at lower speeds if the waves are steep enough.

In order to assure safe operation of vessels, recommendations are needed for their heading and speed in terms of sea conditions for $H_s$ and $T$. These recommendations should be given such that the risk of a dangerous situation is small. Assuming that each apparent wave during a fixed sea state have equal risk of causing a broaching-to capsize scenario, that the risk of such an event happening is small for each individual apparent wave, and that apparent waves are nearly independent, the time from the start of the journey to the first broaching-to scenario will be exponentially distributed (Poisson approximation of a binomial distribution). Hence, the risk will be measured by the capsize intensity which will depend on the type of ship and operating conditions such as sea state, heading, and speed. We summarize the operating conditions in a vector of parameters, $\theta = (H_s, T_z, \phi, v)$, where $\phi$ is the angle between the heading of the ship and the direction of the traveling waves, and $v$ is the speed of the ship. The angle, $\phi$, is estimated in the same way as in the fatigue example.

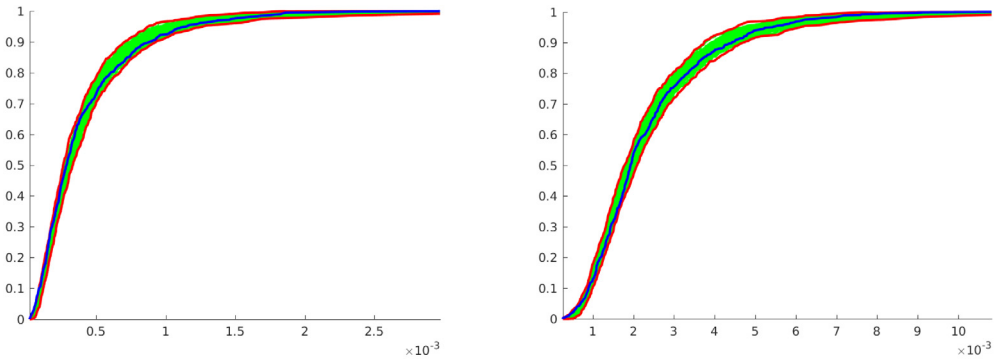

(a) From USA to Europe. (b) From Europe to USA.

**Fig. 16.** Empirical CDFs of accumulated fatigue damage for the transatlantic route. Empirical CDF from data (blue line), 200 different empirical CDFs from simulations (green), and pointwise upper and lower envelopes of the simulated CDFs (red). (For interpretation of the references to color in this figure legend, the reader is referred to the web version of this article.)

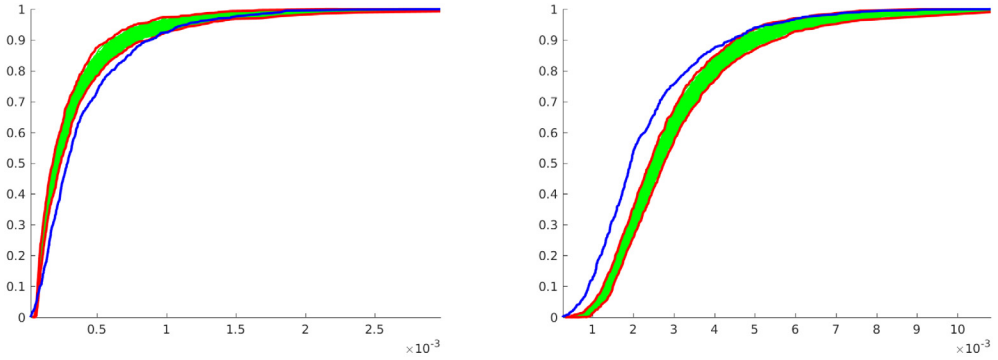

(a) From USA to Europe. (b) From Europe to USA.

**Fig. 17.** Results for accumulated fatigue damage as in Fig. 16 but where the univariate spatial model of $H_s$ was used together with the proxy $T_z(\boldsymbol{s}) = 3.75\sqrt{H_s(\boldsymbol{s})}$.

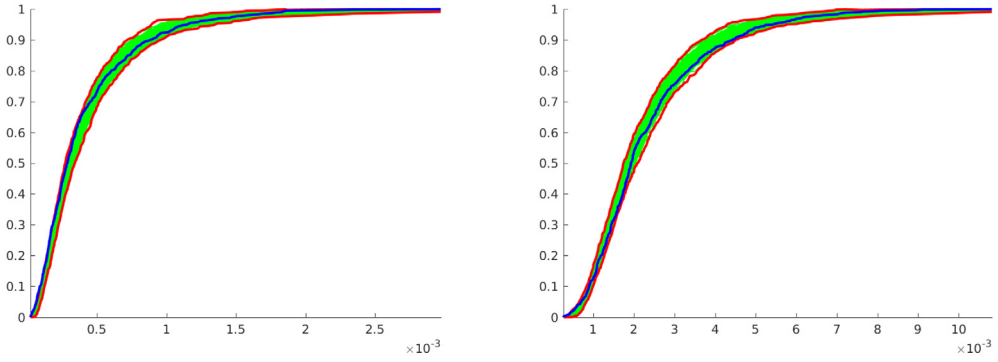

(a) From USA to Europe. (b) From Europe to USA.

**Fig. 18.** Results for accumulated fatigue damage as in Fig. 16 but where the univariate spatial model of $H_s$ is used and $T_z$ is the conditional mean given $H_s$ (when using the pointwise ML estimate).

Let $\lambda(\theta)$ denote the Poisson intensity, meaning the expected number of capsizes in given time unit under the operational conditions $\theta$. In order to estimate capsize probability a detailed understanding of what constitutes a "dangerous wave" is necessary, i.e., what geometrical properties make it more likely to cause capsize when it overtakes a vessel from behind. Further, it seems likely that the probability of such a wave causing a capsize will depend on factors such as the position and motion of the vessel relative to the overtaking wave when an encounter is initiated. Simulations on the performance of a coast guard cutter in severe sea conditions, run by the U.S. Coast Guard, was studied in [37]. For capsizes due to broaching-to the vessel track of the simulated ship along with the shape of the last wave preceding the capsize event, which we refer to as the "triggering wave", were recorded. A common denominator of the triggering waves is the similar (steep) slope between peak and trough. It is therefore reasonable to define a wave as dangerous if its downward slope lies within some range of steep slopes as the wave passes the center of gravity of the vessel. We then want to calculate the rate, $\mu_D(\theta)$, in which dangerous waves are expected to overtake the vessel, and further adjust this by the estimated probability that a dangerous wave will cause a capsize.

#### 6.2.1. Intensities of potentially dangerous overtaking waves

A monochromatic plane wave has wavelength $L = 2\pi g/\omega^2$, period $2\pi\omega^{-1}$, and velocity $V = L/T$. For the ship traveling with speed $v > 0$ and an angle of $\phi \in [-\pi/2, \pi/2]$ to the propagating direction of the wave the intensity of overtaking waves is $\mu(\theta) = (V - v_x)^+/L$. Here, $v_x = v\cos(\phi)$ and $a^+ = \max(a, 0)$. Note that a wider angle between the heading of the vessel and the wave direction yields a higher intensity. Likewise, a smaller ship speed also yields a higher intensity. At the same time, too large values of $\phi$ will not cause dangerous broaching-to events since the heading of the ship will not change dramatically; although encountering big waves perpendicular to the heading of a ship can be dangerous for other reasons.

Similarly to the monochromatic wave the intensity of an apparent wave overtaking the center of gravity of the ship in a non-degenerate Gaussian sea has been shown to be [39],

$$\begin{aligned}\mu(\theta) &= \mathbb{E}\left[\frac{(V - v_x)^+}{L}\right] \\ &= \frac{1}{4\pi}\sqrt{\frac{m_{20}}{m_{00}}}\left(-\frac{m_{11}}{m_{20}} - v_x + \sqrt{v_x^2 + 2\frac{v_x m_{11}}{m_{20}} + \frac{m_{02}}{m_{20}}}\right),\end{aligned} \tag{7}$$

where

$$m_{ij} := \int_0^\infty \left(\frac{\omega^2}{g}\right)^i \omega^j S(\omega) d\omega$$

are the spectral moments of the Gaussian process.

A ship being overtaken by an apparent wave is only dangerous if the wave is high and has a steep slope. Analytic derivations [1, Theorem 6.2] give an explicit formula for the CDF of $W_x(x_0, t_0)$, where, $x_0, t_0$ are instances in space–time where the center of gravity of the ship is being overtaken by the zero level down-crossing of an apparent wave, and $W_x$ is the partial derivative of $W$ with respect to the spatial direction of the propagating wave. The formula for the CDF is

$$F_{W_x}(r) = \begin{cases} \frac{2}{1-\rho}\left(\Phi(r/\sigma) - \rho\, e^{-\frac{r^2}{2m_{20}}}\Phi(r\rho/\sigma)\right) & \text{if } r \le 0, \\ 1 & \text{if } r > 0. \end{cases} \tag{8}$$

Here, $\Phi(x)$ is the CDF of the standard normal distribution, $\sigma^2 = m_{20}(1 - \rho^2)$, and

$$\rho = \frac{v_x m_{20} + m_{11}}{\sqrt{m_{20}(v_x^2 m_{20} + 2v_x m_{11} + m_{02})}}.$$

The intensity of a broaching-prone wave scenario is the product of the intensity of overtaking waves thinned with the probability that the overtaking wave has a dangerously steep slope, i.e.,

$$\mu_D(\theta) = \mu(\theta)\mathbb{P}\left(W_x(x_0, t_0) \in A\right),$$

where $A$ is an interval of slopes considered dangerous. Inspired by Leadbetter et al. [37], we choose $A = [-0.4, -0.2]$.

Since the spectral moments are known functions of $H_s$ and $T$, assuming a Bretschneider spectrum, we can compute them for each point on the route for a given realization of $H_s$ and $T$. In the following example we computed the spectral moments assuming a limited bandwidth and numerical integration using the Matlab toolbox WAFO [3]. Using the route of Fig. 15(a) and wave directions of Fig. 15(b), $\mu_D(\boldsymbol{s}_\gamma(t))$ can be estimated conditioned on a given sea state scenario using (7) and (8).

#### 6.2.2. Estimation of $\lambda(\theta)$ response surfaces

Conditioned on the ship being overtaken by a "dangerous" wave the capsizing phenomenon is a result of complicated nonlinear interactions between the wave and the vessel. Direct computations of risk for capsizes based on random models for sea motion and vessel response are not feasible to obtain. In addition, there are limited data of capsizing available. Consequently one must study the problem using tank experiments with model ships or by means of computer simulations of the responses. Since a capsize due to broaching-to occurs with a small probability tank experiments would require too much time to get stable estimates of the capsize probability for all but the most severe sea states. Instead, appropriate computer simulations are the best methods for estimating the probability of capsize and related events under moderately high sea conditions.

Leadbetter et al. [37] derived a method for modeling the capsizing intensity due to broaching-to, $\lambda$, based on Poisson regression on the covariates $\mu_D$, $H_s$, and $T_1$, i.e.,

$$\lambda(\theta) = \mu_D(\theta)\exp\left(\beta_0 + \beta_H \log H_s + \beta_T \log T_1\right).$$

The values of $\beta_0, \beta_H$, and $\beta_T$ depend on the ship type in consideration; a heavier and larger ship can withstand taller waves without broaching-to, as compared to a small ship. The parameters of the regression for a U.S. coast guard cutter were estimated in [37]. It turned out that this standard linear Poisson regression satisfactorily explained $\lambda(\theta)$ with the parameters $\beta_0, \beta_H$, and $\beta_T$ estimated from capsize data in the computer simulations. The values were $\beta_0 \approx \log(0.05), \beta_H \approx 7.5$, and $\beta_T \approx -7.5$. The model was shown to predict intensities of order $10^{-3}$ adequately. It is still not known if the model can be extrapolated to even safer operating conditions. However, the predicted sea states that should be avoided are in line with the ones found using significant roll threshold, see [37, Fig. 22.2].

For a ship traversing the route of Fig. 15(a), $\lambda(\theta(\boldsymbol{s}_\gamma(t)))$ is the conditional capsize intensity of an inhomogeneous Poisson process over the space–time curve of the ships path given the sea states, $\theta$. The distribution of capsizes, if assuming that a ship could continue after a capsize, would then be Poisson distributed with intensity,

$$\lambda(\theta) := \int_0^{t_{end}} \lambda(\theta_\gamma(t))dt \approx \sum_{i=1}^{100} \lambda(\theta_\gamma(t_i))\Delta t,$$

where $\theta_\gamma(t) := \theta(\boldsymbol{s}_\gamma(t))$. The capsize events can hence be considered as a Cox process where the latent random intensity is given by the sea states, $\theta$.

In our example we compute the distribution of $\lambda$ as a function of the bivariate random field $H_s, T$. We use the same coefficients as in Leadbetter et al. [37], i.e., $\beta_0 = \log(0.05), \beta_1 = 7.5, \beta_2 = -7.5$. When computing $\lambda$ we consider traversing the route from America to Europe with the wave directions as in Fig. 15(b). Furthermore, we choose the cutoff angle, $\phi_0 = 75°$, meaning that we only consider waves as potentially dangerous if the angle between the ships heading and the propagation direction of the waves are less than $\phi_0$. The scenario of traversing the route from Europe to America was not considered since the wave direction angle was always more than $\phi_0$, i.e., negligible risk of a dangerous apparent wave overtaking the ship from behind.

The distribution of capsize intensities, $\lambda$, as well as corresponding total intensities of overtaking waves and dangerous overtaking waves can be seen in Fig. 19. The figure shows the estimated CDF of the total intensities, $\mu$, $\mu_D$, and $\lambda$, for a ship traversing the transatlantic route of Fig. 15(a) from America to Europe. The left column correspond to computations using the proposed bivariate spatial random model of sea states. The right column correspond to the simpler model of the univariate spatial $H_s$ model together with the pointwise conditional mean of $T$, which was found to be sufficient for the fatigue application in Section 6.1. The CDF computed from the data is compared with 20 simulations of the same size as the data, that is 600 days.

As can be seen in Fig. 19, the simpler model is now clearly deviating from the empirical CDF of the data. The proposed bivariate spatial model show a better fit although it seems to overestimate the risks slightly for medium sized intensities. Thus, for this application the bivariate model is clearly outperforming the simpler alternative.

## 7. Discussion

A joint spatial model of significant wave height and wave period has been introduced. The model is a bivariate extension of the model of Hildeman et al. [17] using the multivariate random field approach

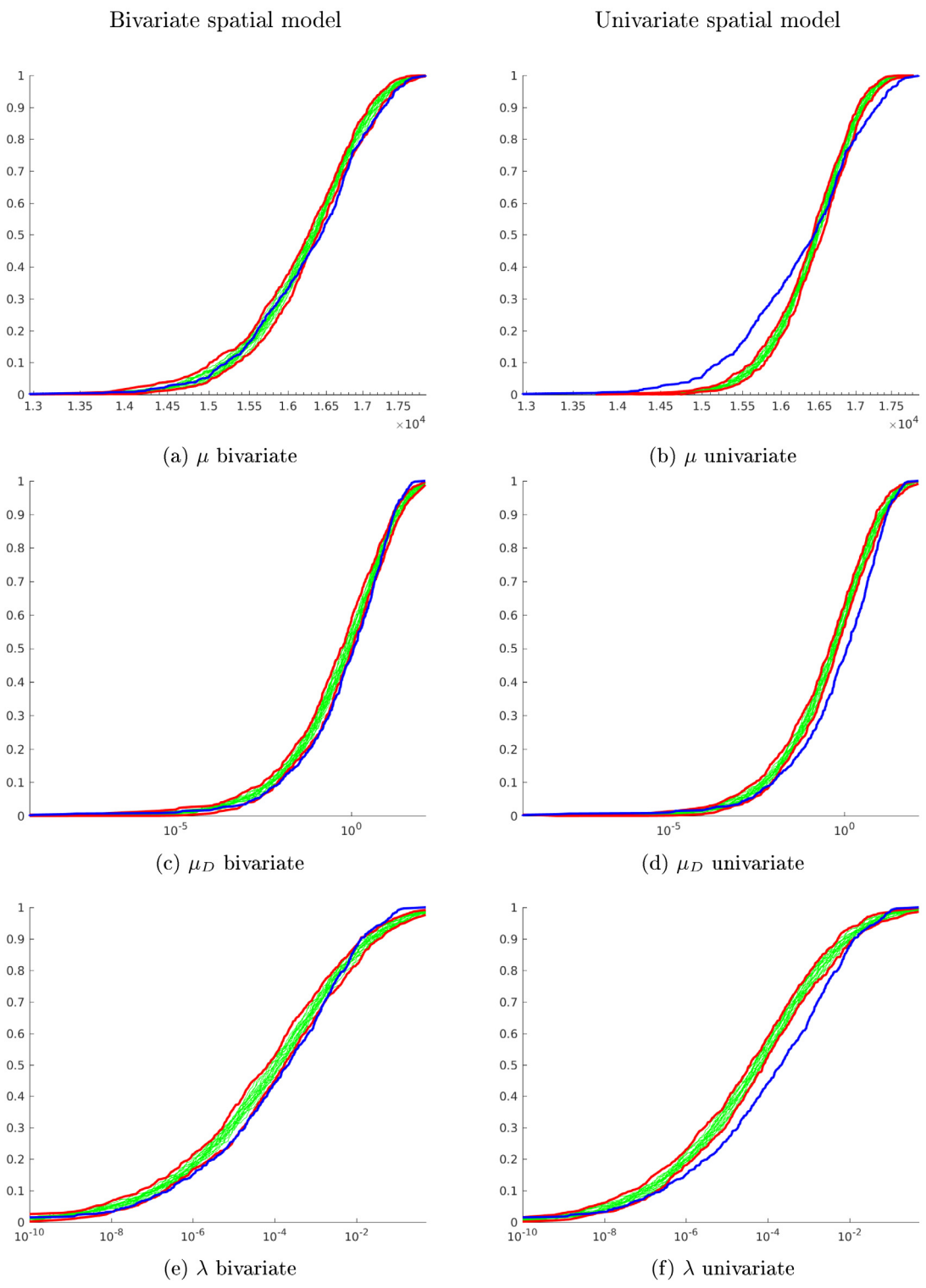


**Fig. 19.** Empirical CDFs of total $\mu$, $\mu_D$, and $\lambda$. The broaching-to risks were computed using two different models of sea states, the proposed bivariate random field model (left) and the simpler model of spatial $H_s$ with the marginal conditional mean of $T$ (right). Empirical CDF from data (blue), corresponding empirical CDFs from 20 simulations (green) and the pointwise upper and lower envelopes of the empirical CDFs (red). (For interpretation of the references to color in this figure legend, the reader is referred to the web version of this article.)

of Bolin and Wallin [21],Hu et al. [22]. Furthermore, the model also incorporates the rational approximation to Matérn fields of arbitrary smoothness [25]. This means that the spatial model allows for non-stationary, anisotropic models of bivariate Gaussian random fields, each with its own arbitrary smoothness. The model is parametrized with a relatively small number of easily interpretable parameters.

The model was fitted using data from the month of April from the ERA-Interim global atmospheric reanalysis [29]. A stepwise maximum likelihood approach together with numerical optimization by a quasi-Newton method was used to estimate the parameters of the model. The univariate models for $H_s$ and $T$ separately agrees well with data. However, problems were encountered when fitting the cross-correlation

structure between $H_s$ and $T$. The problem is that the cross-correlation is not at its maximum between the same spatial points in $H_s$ and $T$, as assumed by the model. This lead to ML estimates of the cross-correlation structure that did not agree at all with the observed data. Instead, estimating the cross-correlation structure using a pointwise maximum likelihood method yielded better results; although the cross-correlation was clearly underestimated for long distances.

The shift of locations of maximum cross-correlation, as seen in Fig. 11, is likely an effect of the dynamic nature of ocean waves and their interaction with wind. It is known from naval architecture practice that transitions from low sea states to high sea states, so called "rising sea", are often more dangerous than the high sea states themselves. This is because during a rising sea the significant wave height can be high while the mean wave period is small, leading to steeper waves. This is in accordance with Fig. 10 suggesting $T$ as lagging $H_s$ in the direction of the flow. Since the proposed model assumes a symmetric cross-correlation structure with maximum cross-correlation between the same point in the two fields it cannot accommodate this property of the joint distribution of $H_s$ and $T$. Due to the shifts, the real cross-correlation is not symmetric. It would make sense to incorporate these shifts into the bivariate model, using the model of Li and Zhang [40] for instance. This is an interesting extension of the multivariate modeling approach using systems of SPDEs and was proposed in [23]. Such shifts could be considered as a diffeomorphism between $\mathcal{G}$ and some overlapping region $\mathcal{H}$. This diffeomorphism would fulfill that when $\log T$ is mapped to $\mathcal{H}$, the two fields, $\log H_s$ and $\log T$, align, i.e., maximum cross-correlation is between the same point in the two fields. The proposed model of this paper could then be applied to this transformed data. An even better solution would be to model $H_s$ and $T$ spatio-temporally. A velocity field corresponding to the "flow of sea states" would define a Lagrangian frame of reference. Then, the point of maximum cross-correlation could simply be defined as $T$ lagging an appropriate amount of time in the Lagrangian frame of reference.

The spatial model was evaluated in two applications in naval logistics. Both applications considered risks of undertaking a journey between the European and American continents through the north Atlantic. The first application considered computing the probability distribution of accumulated fatigue damage acquired during the journey. It was shown that the spatial model agreed with data. In particular, it showed that it works better than the approach where $T_z$ is replaced by the proxy $T_z = 3.75\sqrt{H_s}$, which was used in [17]. However, a simpler model using only the univariate spatial random field model of $H_s$ together with pointwise conditional means of $T$ given $H_s$ yielded an adequate fit as well.

The second application concerned the risk of capsizing due to broaching-to. An inhomogeneous Poisson process was derived given the bivariate sea state surface of $H_s$ and $T$. The Poisson intensity depended on the intensity of the ship being overtaken by a wave from behind, the probability that the overtaking wave is steep, and a Poisson regression of the probability of capsizing given a dangerous wave. The distribution of capsizing intensity (corresponding to the risk of capsizing) was compared between the proposed bivariate spatial model and the data. The spatial model showed a reasonable fit but seems to overestimate the risk slightly. The simpler model, using the univariate random field of $H_s$ from [17] together with the pointwise conditional mean of $T$, was on the other hand clearly deviating from the distribution of the data. This shows that the bivariate model is indeed important for certain applications and cannot simply be substituted by simpler univariate models. It should be mentioned that the evaluated risks of capsizing are conservative estimates. Actual capsizing of a large ship involves many additional events, such as cargo shifts, hull damage, human errors, dislocation of main engines and other heavy-machinery. An interesting future extension of the risk assessment for broaching-to is that to risks of high-runs. This extension could be based on the work of Kontolefas and Spyrou [41]. High-runs are a similar but more general phenomenon than broaching-to where a ship can loose steering and experience quick and uncontrolled yaws due to complex ship–wave interactions.

## Declaration of competing interest

The authors declare that they have no known competing financial interests or personal relationships that could have appeared to influence the work reported in this paper.

## Acknowledgments

We would like to thank the European Centre for Medium-range Weather Forecast (ECMWF) for the development of the ERA-Interim dataset and for making it publicly available. The data used was the ERA-Interim reanalysis dataset, Copernicus Climate Change Service (C3S) (accessed September 2018), available from "https://www.ecmwf.int/en/forecasts/datasets/archive-datasets/reanalysis-datasets/era-interim".

## References

[1] S. Åberg, I. Rychlik, M.R. Leadbetter, Palm distributions of wave characteristics in encountering seas, Ann. Appl. Probab. 18 (3) (2008) 1059–1084.
[2] C.L. Bretschneider, Wave Variability and Wave Spectra for Wind Generated Gravity Waves, Technical Report 118, Beach erosion board, Corps of engineers, 1959, p. 196.
[3] P.A. Brodtkorb, P. Johannesson, G. Lindgren, I. Rychlik, J. Rydén, E. Sjö, Wafo - A matlab toolbox for analysis of random waves and loads, in: Proc. 10th Int. Offshore And Polar Eng. Conf., Seattle, vol. 3, 2000, pp. 343–350.
[4] M.K. Ochi, On the long-term statistics for ocean and coastal waves, in: Proc. 16th Conf. Coastal Engineering, vol. 1, 1978, pp. 59–75.
[5] R.L. Placket, A class of bivariate distributions, J. Am. Stat. Assoc. 60 (310) (1965) 516–522.
[6] G.A. Athanassoulis, E.K. Skarsoulis, K.A. Belibassakis, Bivariate distributions with given marginals: With an application to wave climate description, Appl. Ocean Res. 16 (1995) 1–17.
[7] G.E.P. Box, D.R. Cox, An analysis of transformations, J. R. Stat. Soc. Ser. B (1964) 211–252.
[8] C. Guedes Soares, Long term and extreme value models of wave data, in: Marine Technology And Engineering, CRC Press, 2011.
[9] C. Lucas, C. Guedes Soares, Bivariate distributions of significant wave height and mean wave period of combined sea states, Ocean Eng. (2015) 341–353.
[10] E. Vanem, Joint statistical models for significant wave height and wave period in a changing climate, Mar. Struct. 49 (2016) 180–205.
[11] V. Monbet, P. Ailliot, M. Prevosto, Survey of stochastic models for wind and sea state time series, Probab. Eng. Mech. 22 (2007) 113–126.
[12] A.B. Degtyarev, A.M. Reed, Synoptic and short-term modeling of ocean waves, Int. Shipbuild. Prog. 60 (2013) 523–553.
[13] A.B. Degtyarev, New approach to wave weather scenarios modeling, in: Contemporary Ideas on Ship Stability and Capsizingin Waves, 2011, pp. 599–617.
[14] A. Baxevani, S. Caires, I. Rychlik, Spatio-temporal statistical modelling of significant wave height, Environmetrics 20 (2009) 14–31.
[15] A. Baxevani, I. Rychlik, R.J. Wilson, A new method for modelling the space variability of significant wave height, Extremes 8 (2005) 267–294.
[16] P. Ailliot, A. Baxevani, A. Cuzol, V. Monbet, N. Raillard, Space-time models for moving fields with an application to significant wave height fields, Environmetrics 22 (2010) 354–369.
[17] A. Hildeman, D. Bolin, I. Rychlik, Deformed SPDE models with an application to spatial modeling of significant wave height, Spatial Stat. 42 (2021).
[18] F. Lindgren, H. Rue, J. Lindström, An explicit link between Gaussian fields and Gaussian Markov random fields: The stochastic partial differential equation approach, J. R. Stat. Soc. 73 (4) (2011) 423–498.
[19] P.D. Sampson, P. Guttorp, Nonparametric estimation of nonstationary spatial covariance structure, J. Am. Stat. Assoc. 87 (417) (1992) 108–119.
[20] P. Whittle, On stationary processes in the plane, Biometrika 41 (3/4) (1954) 434–449.
[21] D. Bolin, J. Wallin, Multivariate type G Matérn stochastic partial differential equation random fields, J. R. Stat. Soc. Ser. B 82 (1) (2020) 215–239.
[22] X. Hu, D. Simpson, F. Lindgren, H. Rue, Multivariate Gaussian random fields using systems of stochastic partial differential equations, 2013, arXiv Preprint arXiv:1307.1379v2.
[23] X. Hu, I. Steinsland, Spatal modeling with system of stochastic partial differential equations, WIREs Comput. Stat. 8 (2) (2016) 112–125.
[24] H. Rue, L. Held, Gaussian Markov Random Fields, volume 104, Chapman and Hall, 2005, p. 280.
[25] D. Bolin, K. Kirchner, The rational SPDE approach for Gaussian random fields with general smoothness, J. Comput. Graph. Statist. 29 (2) (2020) 274–285.
[26] D. Bolin, F. Lindgren, Spatial models generated by nested stochastic partial differential equations, with an application to global ozone mapping, Ann. Appl. Stat. 5 (1) (2011) 523–550.

[27] MATLAB, Version R2018B, The MathWorks Inc., Natick, Massachusetts, 2018.
[28] A. Hildeman, Fieldosophy: A toolkit for random fields, 2021, URL https://github.com/andyGFHill/fieldosophy.
[29] D.P. Dee, S.M. Uppala, A.J. Simmons, P. Berrisford, P. Poli, S. Kobayashi, U. Andrae, M.A. Balmaseda, G. Balsamo, P. Bauer, P. Bechtold, A.C.M. Beljaars, L. van de Berg, J. Bidlot, N. Bormann, C. Delsol, R. Dragani, M. Fuentes, A.J. Geer, L. Haimberger, S.B. Healy, H. Hersbach, E.V. Holm, L. Isaksen, P. Kållberg, M. Köhler, M. Matricardi, A.P. McNally, B.M. Monge-Sanz, J.J. Morcrette, B.K. Park, C. Peubey, P. de Rosnay, C. Tavolato, J.N. Thepaut, F. Vitart, The ERA-interim reanalysis: Configuration and performance of the data assimilation system, Q. J. R. Meterological Soc. April (A) (2011) 553–597.
[30] Berrisford, The ERA-Interim Archive Version Version 2.0, Technical Report, ECMWF, Shinfield Park, Reading, 2011, pp. 1–27.
[31] H. Bakka, J. Vanhatalo, J.B. Illian, D. Simpson, H. Rue, Non-stationary Gaussian models with physical barriers, Spatial Stat. 29 (2019) 268–288.
[32] K. Takahashi, J. Fagan, M.S. Chen, Formation of a sparse bus impedance matrix and its application to short circuit study, in: Eigth PICA Conference Proceedings, IEEE Power Engineering Society, 1973, pp. 63–69.
[33] H. Rue, S. Martino, Approximate Bayesian inference for hierarchical Gaussian Markov random field models, J. Stat. Plan. Inference 137 (10) (2007) 3177–3192.
[34] W. Mao, J.W. Ringsberg, I. Rychlik, G. Storhaug, Development of a fatigue model useful in ship routing design, J. Ship Res. 54 (4) (2010) 281–293.
[35] K. Podgórski, I. Rychlik, A model of significant wave height for reliability assessment of a ship, J. Mar. Syst. 130 (2014) 109–123.
[36] A. Baxevani, I. Rychlik, Fatigue life prediction for a vessel sailing the North Atlantic route, Probab. Eng. Mech. 22 (2) (2007) 159–169.
[37] M.R. Leadbetter, I. Rychlik, K. Stambaugh, Contemporary Ideas on Ship Stability: Risk of Capsizing, Springer, 2019, pp. 381–391.
[38] K.J. Spyrou, The nonlinear dynamics of ships in broaching, Marie Curie Fellowsh. Ann. 1 (2000) 1–7.
[39] I. Rychlik, S. Åberg, R. Leadbetter, Note on the intensity of encountered waves, Ocean Eng. 34 (2007) 1561–1568.
[40] B. Li, H. Zhang, An approach to modeling asymmetric multivariate spatial covariance structures, J. Multivariate Anal. 102 (2011) 1445–1453.
[41] I. Kontolefas, K.J. Spyrou, Probability of ship high-runs from phase-space data, J. Ship Res. 64 (1) (2020) 81–97.